Volume 16

LLE Review

Quarterly Report

July–September 1983

Laboratory for Laser Energetics
College of Engineering and Applied Science
University of Rochester
250 East River Road
Rochester, New York 14623

Volume 16

LLE Review

Quarterly Report

Editor: R. Epstein
(716) 275-5405

July–September 1983

Laboratory for Laser Energetics
College of Engineering and Applied Science
University of Rochester
250 East River Road
Rochester, New York 14623

This report was prepared as an account of work conducted by the Laboratory for Laser Energetics and sponsored by Empire State Electric Energy Research Corporation, General Electric Company, New York State Energy Research and Development Authority, Northeast Utilites, The Standard Oil Company, University of Rochester, the U.S. Department of Energy under contract number DE-AC08-80DP40124, and various other United States Government agencies.

IN BRIEF

This volume of LLE Review contains articles on the initial phase of the infrared-to-ultraviolet conversion of OMEGA, experimental and theoretical advances in the laser-fusion effort, improved target fabrication capabilities, developments in the picosecond optics area of the LLE advanced technology program, and on the National Laser Users Facility activity.

The following are some highlights of the work described in this issue:

- The OMEGA frequency-conversion effort achieved a major milestone during this quarter with the activation of six 351-nm-wavelength beams. In the first series of test shots, the system produced up to 305 J of energy at 351 nm, thus surpassing GDL as the most powerful 351-nm laser currently operating.
- The classical theory of thermal heat transport has been extended to include the effects of steep temperature gradients in the presence of strong magnetic fields. Magnetic fields an order of magnitude smaller than those typically observed could have a strong limiting effect on thermal heat conduction.
- By applying an improved statistical ray tracing theory to the propagation of light beams in plasmas with random density fluctuations, it is possible to describe some of the effects of density fluctuations on illumination uniformity and energy absorp-

tion efficiency in terms of the statistical properties of the density fluctuations.

- The automation of the ablation-layer coating process has significantly improved the target fabrication capability at LLE by removing the need for an operator to devote close and prolonged attention to each target being coated and by permitting much more precise layer-thickness control. Another significant advance has been the improvements in the drill, fill, and plug technique pioneered at LLE, which now allow sealing targets with plugs having masses at least two orders of magnitude smaller than the plugs used previously.
- Experiments in the LLE picosecond biophysics facility analyze the energy transitions and deformations of biomolecules by observing their fluorescent responses on very short time scales.
- A new technique developed at LLE allows finely resolved temporal sampling of an electrical signal by using electron pulses to probe the signal field directly. With this approach, signals need not be passed through electro-optic crystals; this gives the new method the advantage of access to signals in free space.

CONTENTS

Robert Peck (left) and Robert Hutchison, engineers in the Experimental Implementation Group, examine a scale model of the OMEGA system as it would be reconfigured for a full 24-beam ultraviolet conversion. The successful activation of the first six ultraviolet beams during this quarter was a major milestone in the laser-fusion effort at LLE.

Section 1
LASER SYSTEM REPORT

1.A GDL Facility Report

During the fourth quarter of fiscal year 1983 (July through September) we continued to operate GDL as a 3ω (351-nm) interaction facility. Shots were taken in support of interaction, shell hydrodynamics, 3ω holography, and x-ray biophysics experiments; the continuing optical-coating damage-testing program; and several NLUF users. A highlight of the quarter was the smooth, efficient running of the facility, with minimal downtime owing to system problems.

A summary of operations in the GDL facility follows:

Interaction Experiments	163
X-Ray Biophysics	44
Damage Testing	139
NLUF Users	69*
System Pointing, Alignment	56
Miscellaneous	9
TOTAL	480

*Included 20 UCLA and Yale shots, 14 Naval Research Laboratory shots, and 35 University of Pennsylvania and University of Connecticut shots.

1.B OMEGA Facility Report

OMEGA operations this quarter consisted of (a) completion of the wavelength conversion of the six-beam "D group" of OMEGA, from an infrared (1054-nm) output to an ultraviolet (351-nm) output, (b) activation of the frequency-converted beams, and (c) target irradiation experiments with 351-nm beams.

By the beginning of the quarter, only the spatial filter modifications had been completed. We spent the month of July assembling crystals into conversion cells and mounting and aligning the beamsplitters, integrating spheres, calorimeters, and photodiodes which comprise the multi-wavelength emission-sensing system (MESS). The MESS system provides the capability of measuring the total IR beam energy, the crystal output energy, and the fractional composition of the output, in terms of first, second, and third harmonics. A block diagram of the MESS system is illustrated in Fig. 1. Further accomplishments during

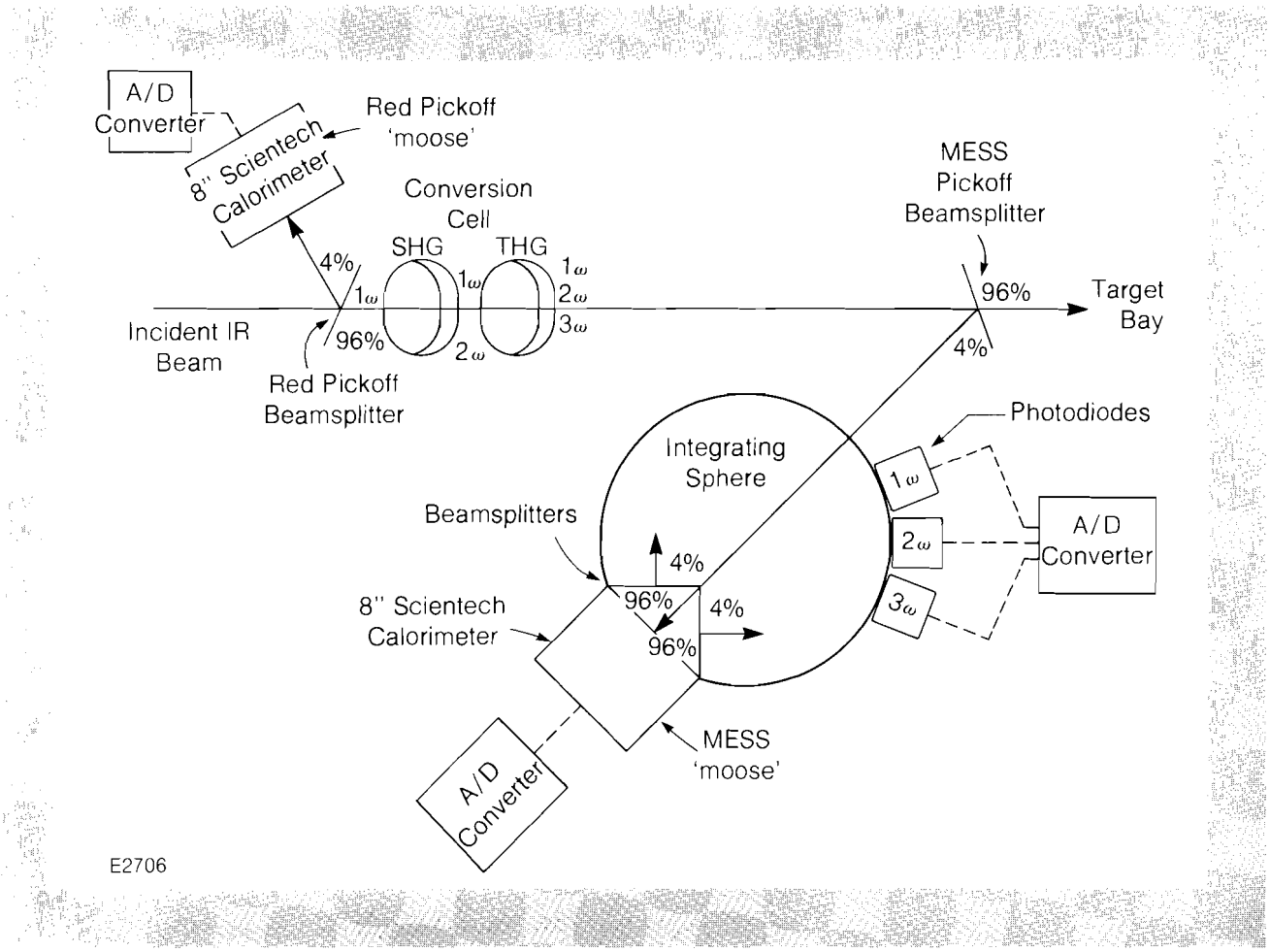

Fig. 1
Multi-wavelength emission-sensing system (MESS) block diagram. The second-harmonic generator (SHG) and third-harmonic generator (THG) crystals are contained within a single cell. The first-, second-, and third-harmonic energy components (1ω, 2ω, and 3ω) of the converted beam are measured individually by photodiodes on an integrating sphere. Total beam energies are measured by calorimeters.

July were the addition of flip-in wave plates in the Pockels-cell structures, to facilitate alignment, and the completion of the thermal control system designed to maintain the crystal cell temperature at ±0.1°C. A majority of the laser system maintenance scheduled for this quarter was completed during July.

In August, we completed the conversion-cell assembly. During the filling of the cells with index-matching fluid, many attempts were required to find a filling technique that would leave no air bubbles remaining in the fluid. As they were completed, the cells were placed

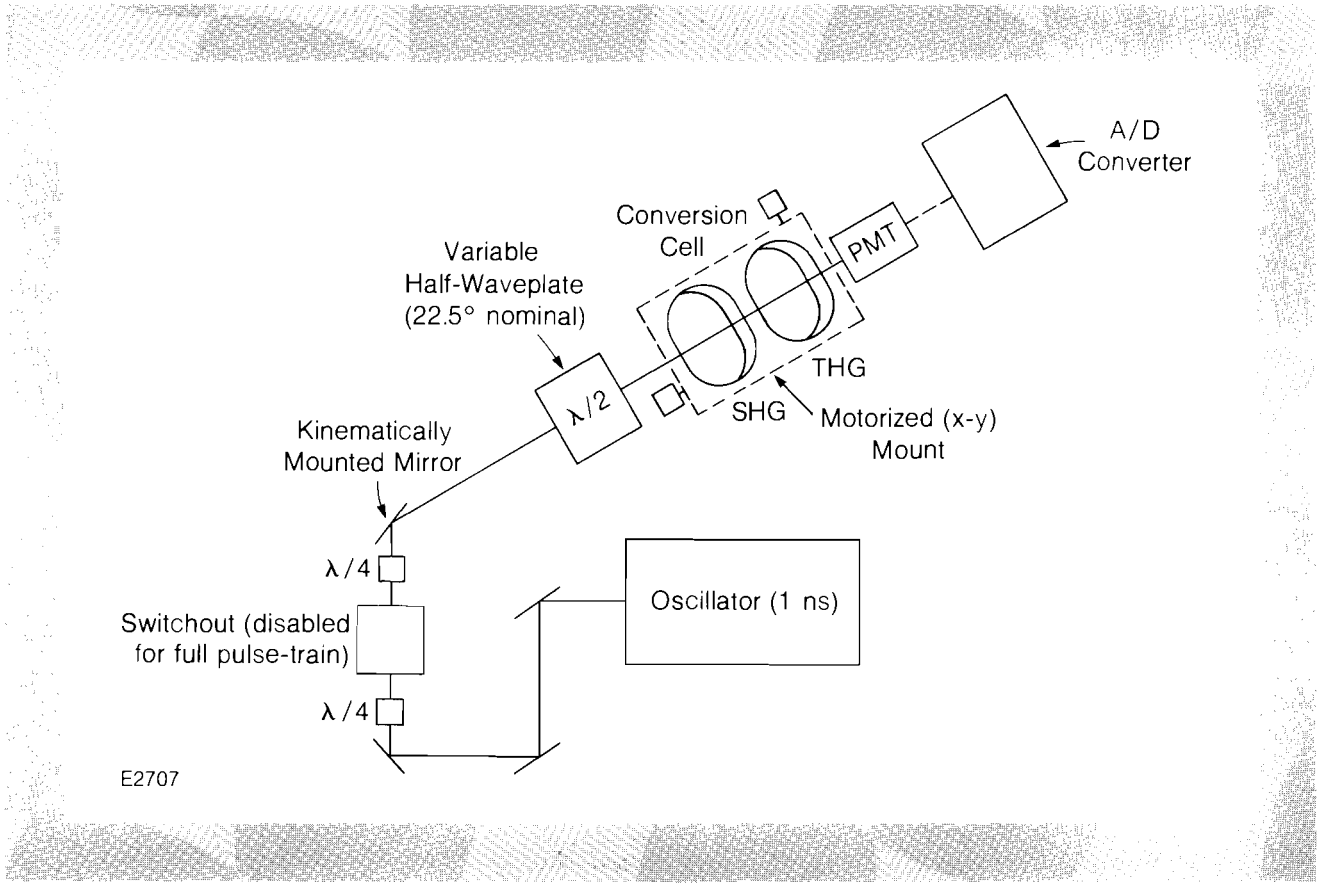

Fig. 2
Driver conversion-cell small-signal tuning setup.

into the small-signal tuning system in the driverline area. Figure 2 shows a schematic of the tuning system. A more complete report describing the automated tuning system is given in the following article. During August, the transport optics were also delivered, and interferometric testing and angular characterization of coatings were performed.

By the end of August, we had completed assembly of the system up to the turning mirrors, and we began activation of the ultraviolet beams. The MESS system was calibrated, using a well-characterized 8-inch Scientech calorimeter, or "moose," as a reference in each beam, and using a subtractive procedure to calibrate the photodiodes. The first ultraviolet energy out of the six beams was measured on 2 September, at a level of approximately 50 J.

During September, we began final preparation for target shots. The first tasks were system maintenance and large-signal tuning of the conversion cells. After the cells were tuned, the energy of the system was increased to measure the maximum energy available in the ultraviolet. Target shots were then taken with the infrared beams, for diagnostic shakedown, and the conversion cells were adjusted for maximum third-harmonic output. By 21 September, the ultraviolet output of OMEGA had been increased to 305 J. Even higher performance is expected as we gain confidence in the performance of the system. Figure 3 shows the performance of the beams, during the activation shots, compared to MIXER[1] code predictions of the conversion.

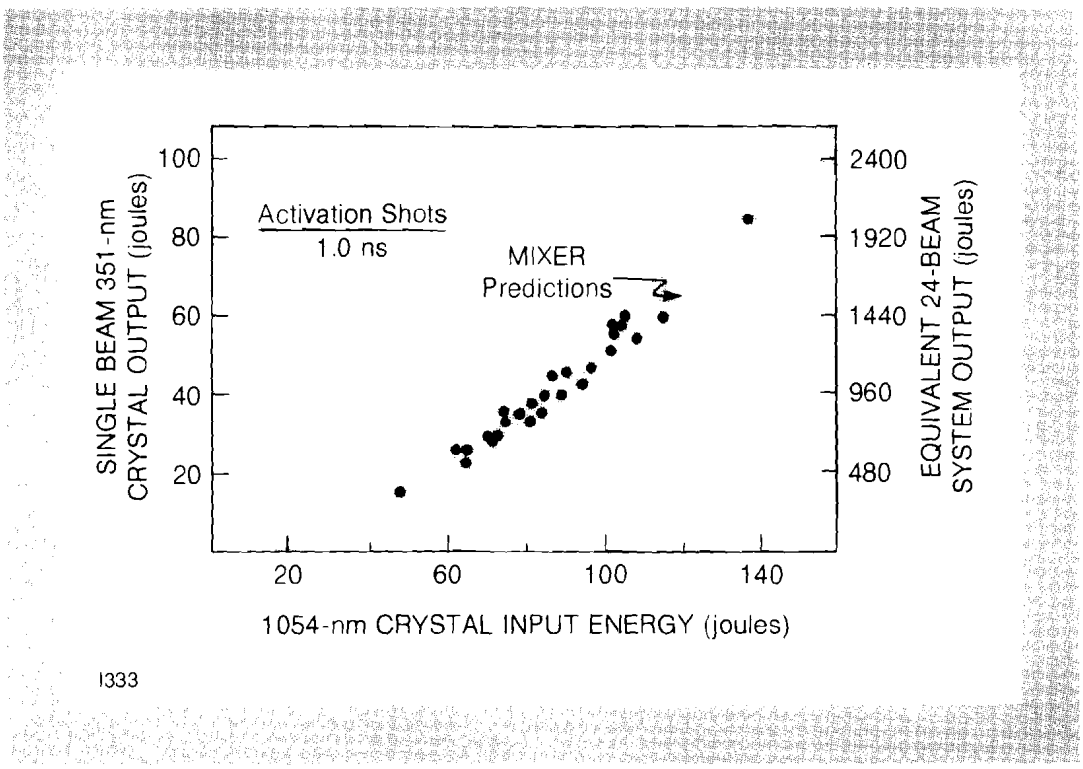

Fig. 3
Ultraviolet conversion efficiency measurements demonstrated close agreement between OMEGA single-beam performance and predictions of calculations using the frequency-conversion code MIXER.[1]

The final weekend of September was spent on (a) installation and alignment of focus lenses, (b) adjustment and check-out of the focus-lens pneumatic-ram system, which rapidly translates the focus lenses from the red focal position along the 33.2-mm distance to the ultraviolet focus position, and (c) realignment of all six beams. Substantial diagnostic activation and checkout work was accomplished during this period, and by the beginning of the final week of this quarter, the first six-beam pointing/focusing target shots on OMEGA had been accomplished. During this final week, one day was devoted to target shots and to the characterization of the transport-optics losses, followed by two days of target shots for absorption, thermal-transport, and fast-electron generation experiments.

A summary of OMEGA operations during this quarter is as follows:

Target Shots	19 @ 3ω
	10 @ 1ω
Ultraviolet Calibration and Tuning Shots	93
Driver Alignment	88
Software Tests, Misfires, Miscellaneous	111
TOTAL	321

REFERENCES
1. R. S. Craxton, *Opt. Commun.* **34**, 474 (1980).

1.C Automated Crystal Tuning for OMEGA Frequency Conversion

The initial phase of the ultraviolet conversion of OMEGA includes adding monolithic frequency-tripling cells[1] to six beams of the laser system. To obtain the maximum ultraviolet conversion efficiency, these cells must be aligned, or "tuned", to within a fraction of a milliradian of their optimum orientation.[2] In previous applications at LLE,[3] this tuning was done manually. We have developed an automated tuning system for the OMEGA system that significantly reduces the time and effort required to perform the initial tuning of the conversion cells. The tripling cells are tuned using pulses from the OMEGA oscillator, which are available at a high repetition rate, before being installed in the OMEGA system.

The Monolithic Frequency-Tripling Cell

The monolithic frequency-tripling cell consists of two type-II-cut KDP crystals mounted within a single fluid-filled cell.[1] The two crystals are oriented with their "ordinary" axes perpendicular to one another, according to the "polarization-mismatch" scheme.[2,4] The first crystal, the "doubler," converts the incident infrared (1054-nm) beam into a beam containing nearly equal photon-number fluxes of infrared and green second-harmonic (527-nm) photons. The second crystal, the "tripler," converts this composite beam into an ultraviolet third-harmonic (351-nm) beam.

Since the indices of refraction of KDP crystals are dependent on propagation direction, the phase-matching or wave-vector conservation condition required for efficient harmonic generation is satisfied only if the input light is incident at a specific phase-matching angle, relative to the optic axis of the crystal. In the weak-signal limit, the conversion efficiency of a crystal falls off with the phase mismatch Ψ as $(\sin\Psi/\Psi)^2$. This phase mismatch is proportional to the angular deviation of the incident beam direction from the phase-matching direction. At the low pulse energies used for tuning, the efficiency of the tripler is halved if this mismatch angle is 0.5 mrad. The doubler is half as sensitive to this separation angle.[5]

The tripling cell is tuned as a unit to its maximum conversion efficiency by rotating the doubler and tripler crystals to their respective phase-matching angles. For a single crystal, this adjustment is made by rotating the crystal about its ordinary axis. Since the two crystals in the tripling cell are mounted with their ordinary axes orthogonal to each other, each crystal in the cell can be tuned independently, without disrupting the tuning of the other crystal.

The Tuning System

In the tuning system, unamplified 1054-nm pulses are fired from the oscillator at a rate of 0.3 Hz through the tripling cell being tested. The second- and third-harmonic outputs from the cell are monitored and recorded through a computer interface. The computer automatically scans the cell alignment angles by driving two stepping motors on the gimbaled mounting of the tripling cell. A schematic diagram of the tuning system is shown in Fig. 4. Plots of the second-and third-harmonic outputs as functions of the alignment angles are displayed on a screen immediately after the outputs are measured. The convenience of this real-time display and the ability of the tuning system to use information from every oscillator pulse allow the operator to optimize the alignment quickly and efficiently. The speed of this operation is limited only by the pulse rate of the oscillator.

The optimum orientation of the tripling cell is specified relative to a "retro" position where a reference surface on the cell is set normal to the oscillator beam axis. This reference orientation can be reproduced in each converted beam in the OMEGA laser. Once the optimum tuning orientation of a tripling cell has been determined using the tuning system, the cell can be placed in the laser system and rotated directly from the retro position to its phase-matched orientation. A final manual adjustment of the installed tripling cells is performed using the OMEGA beam calorimetry and amplified pulses. Once the optimum angles of a given cell are determined, the tuning process need not be repeated, except as a check on the long-term mechanical stability of the cell.

Operation of the Tuning System

The converted green and ultraviolet tripling-cell outputs are monitored by a photomultiplier which is read with a LeCroy 2249 integrating analog-to-digital converter. The stepper motors and photomultipler are interfaced to a DEC LSI 11 computer using the CAMAC[6] instrumentation standard. The computer includes a floppy disk and a color graphics terminal. A stand-alone Forth software[7] system is used to collect, reduce, display, and store the data.

The tripling cell is tuned by first performing a scan about the ordinary axis of the doubler crystal to locate the second-harmonic conversion maximum, and then by scanning the tripling-cell orientation about the ordinary axis of the tripler crystal while monitoring the ultraviolet output. The automated tuning system allows the operator to select the angular step size of the tuning scans and to select the number of pulse readings to be averaged per plotted point. A file system saves the tuning scan results on floppy disk for later

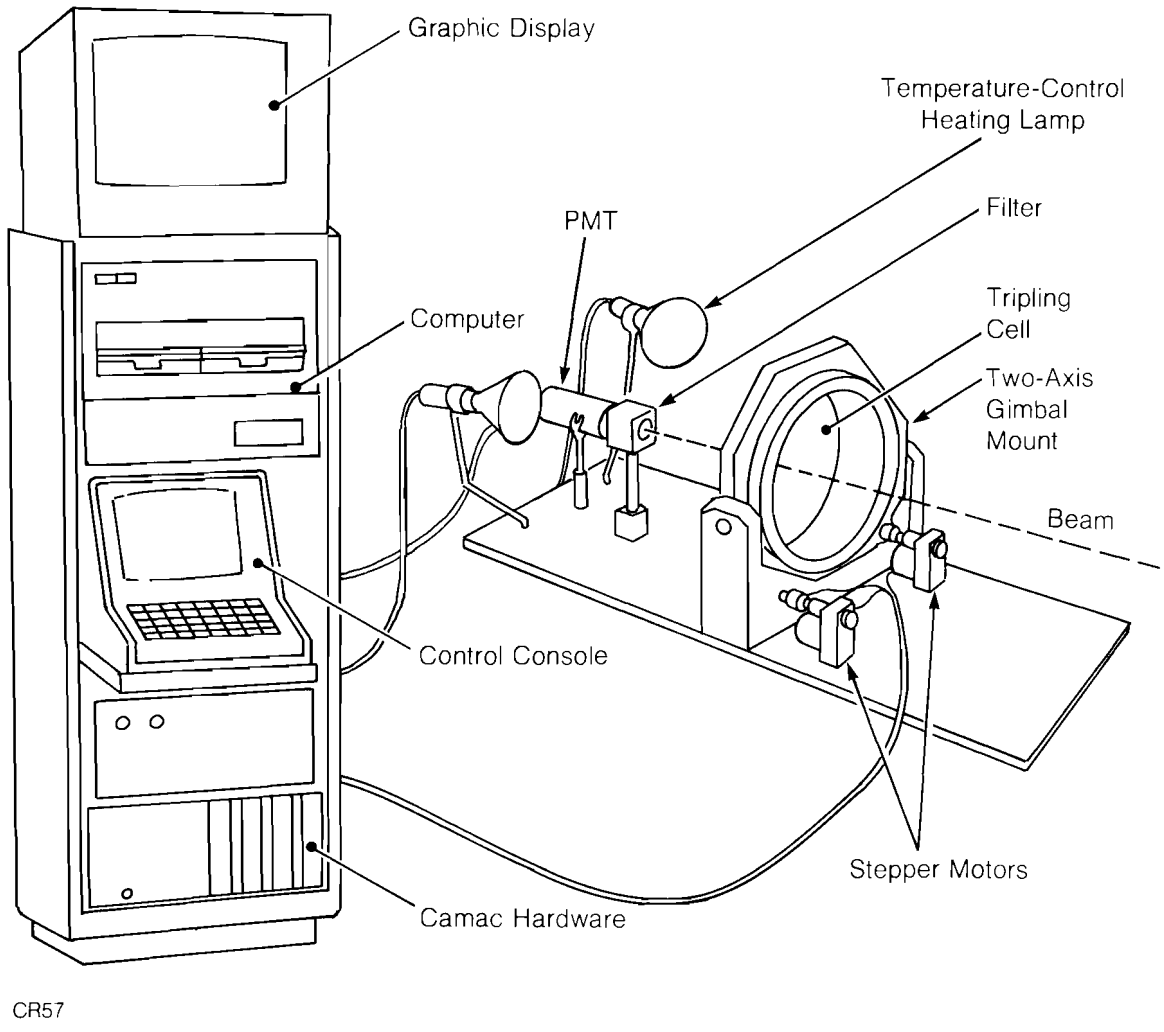

Fig. 4
Diagram of the tuning system showing the basic components.

comparisons or analysis. This allows the triplers to be returned to the testbed to be checked against earlier readings.

Figure 5 shows a typical data display with the color represented as a grey scale. The horizontal graph shows the most recent green scan, and the vertical graph shows the most recent ultraviolet scan. The display includes a color-coded two-dimensional photomultiplier intensity map of the scanning grid, where the two orthogonal rotation axes are represented by a Cartesian grid. This map allows the results of current scans and the stored results of earlier scans to be compared.

For any alignment position, both the green and ultraviolet photomultiplier data can be recorded, but the display shows only the intensities of the harmonic associated with the current scanning angle. Although the computer can be programmed to locate the blue and green maxima, the maxima are currently determined visually by the

operator. The tuning scans must be broad enough to distinguish true maxima from the side lobes of the $(\sin\Psi/\Psi)^2$ modulation of the conversion efficiencies (see Fig. 5).

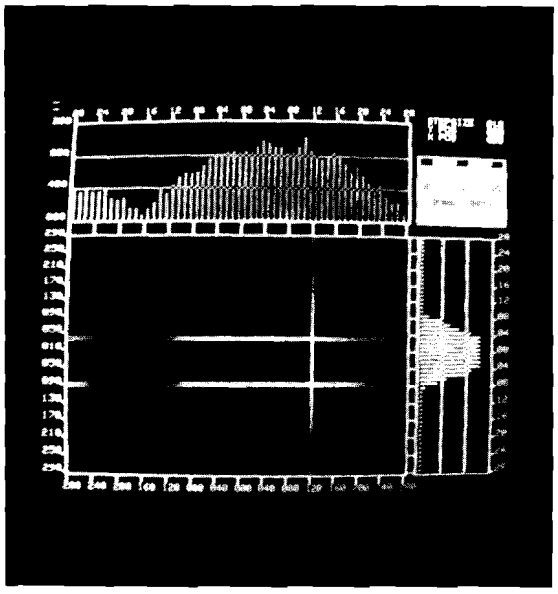

CR58

Fig. 5
Typical scanning display produced by the tuning system. The horizontal and vertical graphs show the results of the current green and ultraviolet tuning-angle scans. The two-dimensional grid (color reproduced as a gray scale) provides a convenient display of both current and stored scan data.

Since the phase-matching angle is strongly wavelength-dependent, one advantage of tuning the tripling cells with the OMEGA oscillator is that both the tuning and operation of the tripling cells are done at the same input wavelength. The phase-matching angle is also strongly temperature-dependent, and, consequently, the temperature of the tripling cells is kept constant to within approximately 0.2°C.

The tuning of all six tripling cells is checked using the OMEGA beam calorimetry after the cells are installed. The conversion efficiencies of the tripling cells are somewhat more sensitive to changes in their tuning angles at the higher powers of the amplified OMEGA pulses than at the lower power used in operating the tuning system. At full power, the peaks can be narrower by nearly a factor of 2.[2] This increased tuning sensitivity, random errors in identifying the initial conversion-efficiency maxima, and errors in reconstructing the tuning-system retro orientation on the OMEGA system are sufficient to require final orientation adjustments of up to a milliradian. The distribution of final angle adjustments shows no evidence of systematic disagreement between the tuning system results and the final tuning angles. The final adjustments of the tripling cells can be expected to require about ten laser shots. In the initial activation of the ultraviolet OMEGA system, the final tuning was completed in the diagnostic-activation shot series.

REFERENCES

1. LLE Review **13**, 30 (1982); M. A. Summers, R. D. Boyd, D. Eimerl, and E. M. Booth, *Technical Digest — CLEO '81, OSA*, p. 30 (June 1981).

2. R. S. Craxton, *IEEE J. Quantum Electron.* **QE-17**, 1771 (1981).

3. W. Seka, J. M. Soures, S. D. Jacobs, L. L. Lund, and R. S. Craxton, *IEEE J. Quantum Electron.* **QE-17**, 1689 (1981).

4. LLE Review **3**, 1 (1980).

5. R. S. Craxton, S. D. Jacobs, J. E. Rizzo, and R. Boni, *IEEE J. Quantum Electron.* **QE-17**, 1782 (1981).

6. "Modular Instrumentation and Digital Interface System (CAMAC)," *IEEE Std.* 583, 1975.

7. M. McCourt, "PDP-11 Forth-79 Implementation Guide," Laboratory for Laser Energetics Computer Systems Group Tech-Notes No. 1, 1981; LLE Review **14**, 48 (1983).

Section 2
PROGRESS IN LASER FUSION

2.A Time-Resolved X-Ray Photography of Imploding Shells

Time-resolved x-ray streak photography and shadowgraphy have long been important diagnostics of dynamic high-density phenomena. Their application to studies of laser-fusion issues permits the space-time analysis of laser-accelerated foils and shells.[1,2] In this section, we describe the development of new high-resolution x-ray photographic instrumentation incorporating x-ray-sensitive, electro-optic image converter tubes,[3] specifically for the purpose of studying the temporal behavior of fusion targets imploded on the OMEGA facility. An earlier x-ray system, developed at LLE in 1977, is described in Ref. 4. Time-resolved x-ray streak photography uses electro-optic streak cameras in conjunction with x-ray imaging to record the time history of that segment of an image of the plasma centered across a slit disposed in front of the photocathode. This system permits the analysis of the high-temperature plasma, while x-ray shadowgraphy with the use of a secondary laser-produced x-ray source allows the motion of cold high-density surfaces to be recorded. These techniques are illustrated schematically in Fig. 6.

The analysis of imploding fusion targets places stringent requirements on temporal and spatial resolution and on alignment accuracy. Although the intrinsic time resolution of a streak camera is limited by the temporal dispersion of the photoelectrons,[5] most time-resolved imaging studies of nanosecond x-ray phenomena are limited by the slit-width/streak-velocity ratio. The slit width should be equal to or larger than the spatial-resolution-element size at the photocathode.

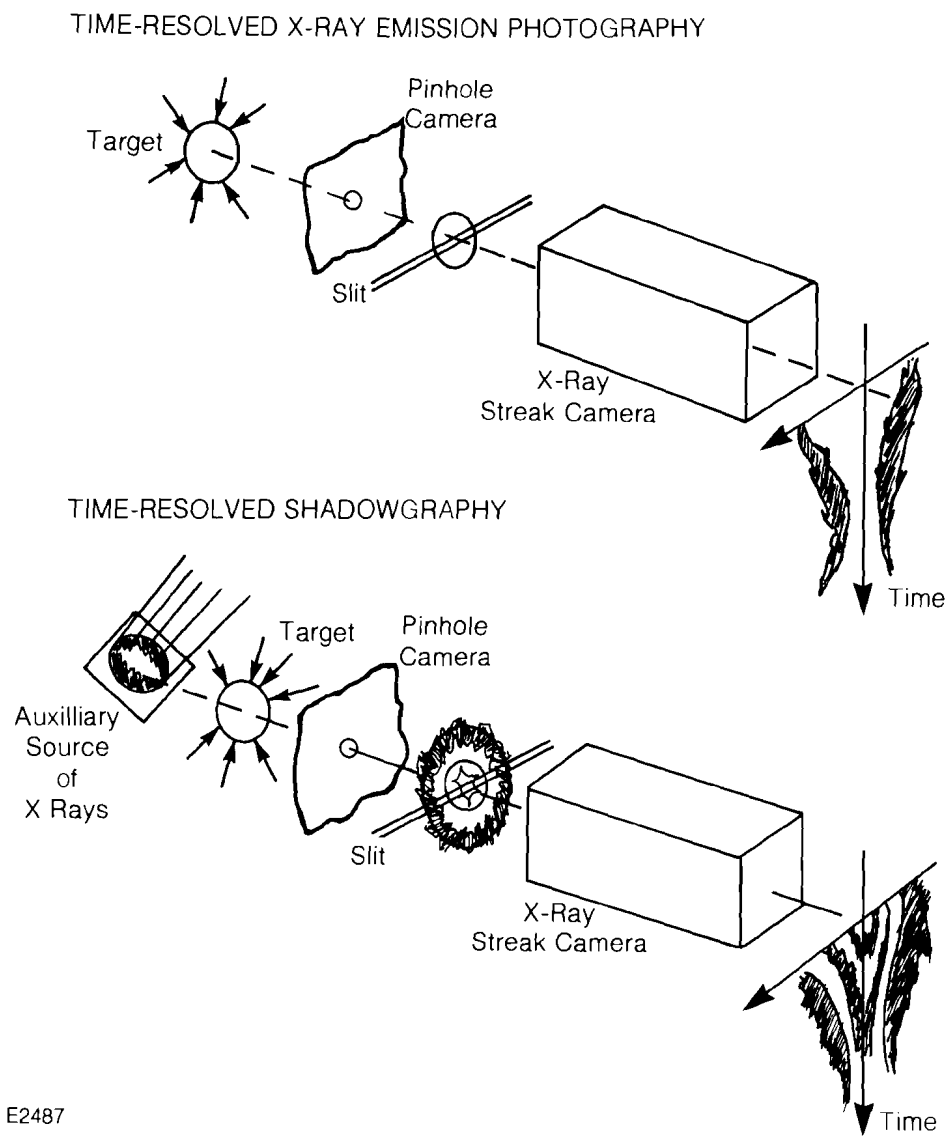

Fig. 6
General configurations for time-resolved x-ray emission photography and time-resolved shadowgraphy.

The latter, together with the number of resolution elements along the length of the slit, and the magnification and pinhole size of the imaging camera used, defines the achievable image spatial resolution. In analyzing the implosion of a spherical target, the relevant parts of the image may shrink by a factor of ~ 10 in spatial scale, and erroneous results will ensue if the slit is not positioned centrally on the final image to high accuracy ($\ll 0.1$ times the original target size). Moreover, the relevance of the resulting data to hydrodynamic simulations of target behavior is considerably increased if the streaked image is related in time to a record of the incident laser pulse, and if there is a known x-ray spectral resolution to the image. These factors are of importance to time-resolved x-ray studies of spherical targets imploded by the 24-beam OMEGA laser system.

The initial tests of this new photographic system were made with the OMEGA facility configured to provide nanosecond, 1053-nm kilojoule pulses. These conditions were required for the study of the implosions of gas-filled glass-shell targets of diameters up to 670 μm and having initial aspect ratios up to 250, under conditions of high irradiation symmetry.[6] Time-resolved photographic studies have been made with a streak pinhole camera system having high temporal and spatial resolution (20 ps and 10 μm in the target plane, respectively) and a sensitive pinhole-streak slit alignment system. In the future, this photographic system will be used for time-resolved x-ray studies of high-density implosions driven by multiple-beam, 351-nm laser light from OMEGA, and will include a temporal record of the laser pulse on the recorded streak image.

Time-Resolved Imaging System

The spherical target implosions studied with the OMEGA laser facility were of targets of initial diameter 100-500 μm. They achieved implosion velocities in excess of 10^7 cm/s and collapsed to final core dimensions of 10-60 μm, which required temporal analyses of 2- to 3-ns duration with a time resolution of ~20 ps. The system constructed for time-resolved x-ray photographic studies of these implosions incorporates a pinhole camera assembly and a custom-built x-ray streak camera. The design of the overall system is shown in Fig. 7. Images of the x-ray emission from the target region in the center of the 172-cm-diameter vacuum chamber are produced by a 7-μm pinhole on the photocathode of the streak camera, situated 70.2 cm from target, with a magnification which can be varied from 10 to 25. Thus, the image size can be optimized to the 8-mm-wide photocathode in order to use the limited number of spatial resolution elements to obtain the maximum spatial resolution in the target plane. Lateral movement of the pinhole assembly along two orthogonal axes is allowed with the strong helical flexible coupling of the pinhole assembly to the camera body with mechanical control from outside the vacuum wall. The streak camera has the basic electron-optical geometry of the Photochron II design.[7] However, considerable redesign of the individual electrostatic-field lens elements has been undertaken in order to improve stability, accuracy of alignment, and overall spatial resolution of the image-converter tube. A photograph of the streak-camera system and the pinhole camera assembly is shown in Fig. 8. Image intensification was provided by a 40-mm-diameter, electrostatically focused image intensifier, with fiber-optic coupling to the streak-tube phosphor and to the film holder.

Temporal calibration of the streak was made with the aid of the upconverted, fourth-harmonic (250-nm), single-pulse output of a mode-locked Nd:YLiF laser. This 50-ps pulse was injected into a 240-ps rattle-plate etalon which generated a train of pulses to illuminate the photocathode of the streak camera. The deflection sensitivity established from these studies was 170 ps/mm, with a linearity in the streak velocity of ~10%.

Spatial resolution in the static mode was estimated by illuminating a double-mesh structure situated immediately in front of the photo-

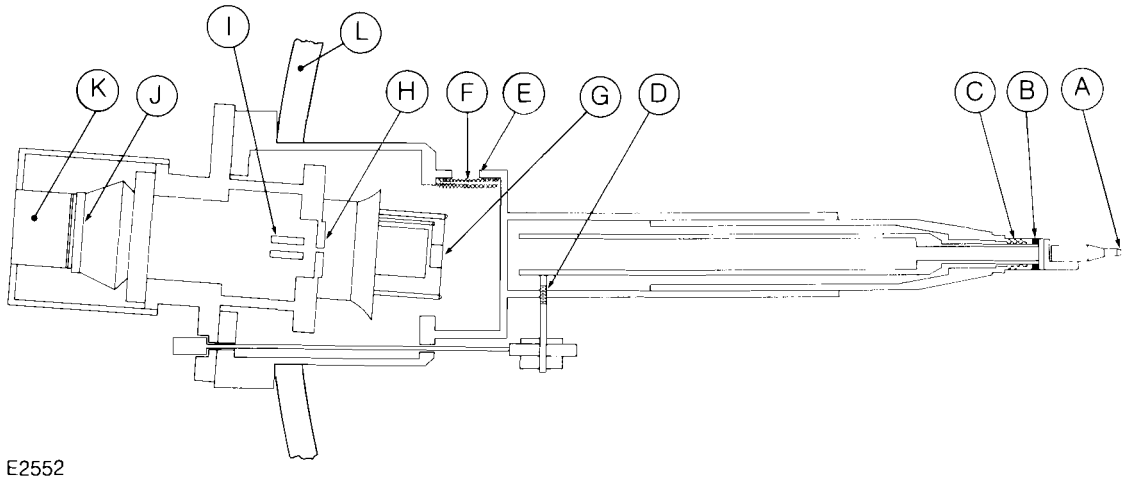

Fig. 7
Details of x-ray-imaging streak camera system. Legend: A-pinhole; B-ion deflection magnets; C-flexible coupling; D-pointing adjustment; E-streak camera pump-out port; F-ion shield; G-photocathode and acceleration grid assembly; H-anode; I-deflection electrodes; J-phosphor; K-image intensifier; L-vacuum tank wall.

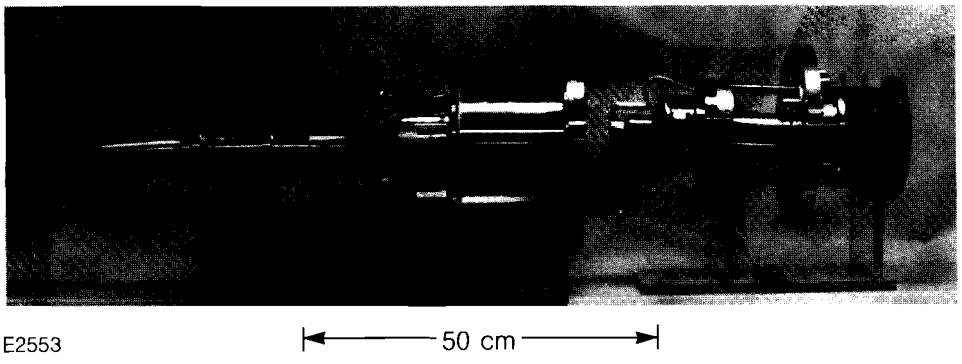

Fig. 8
Photograph of the x-ray-imaging streak camera assembly.

cathode with UV radiation from a cw D_2 lamp ($\lambda \sim 220$ nm). The coarse grid shown in Fig. 9(a) gives an indication of the degree of image distortion imposed by the electrostatic lenses in the streak tube and in the image intensifier. Within the coarse grid structure can be seen the clearly resolved fine structure (16 grid lines/mm) of the fine grid mesh [Fig. 9(b)]. This indicates that, in the static mode, the spatial resolution is somewhat better than 16 grid lines/mm. As will be seen below, this

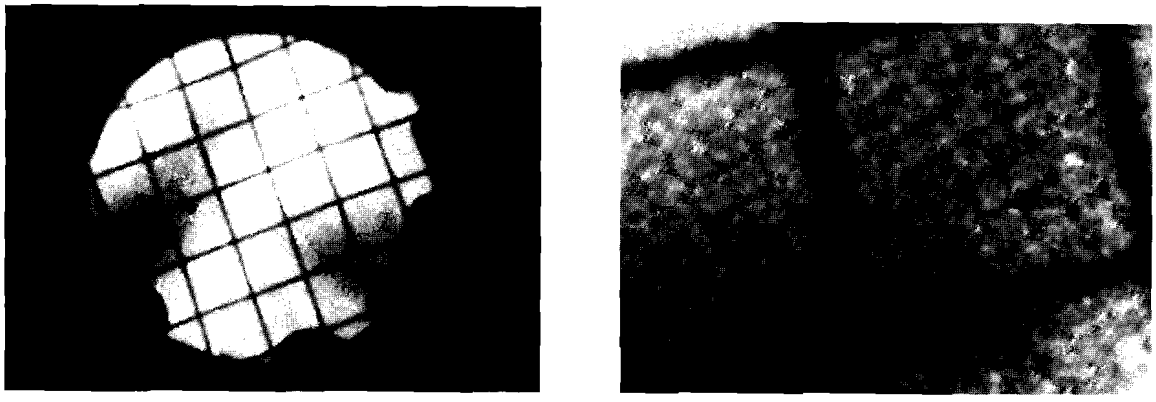

(a) Coarse Grid Spacing 1.2 mm

(b) Fine Grid Spacing 62 μm

E2554

Fig. 9
Static resolution tests of x-ray camera with UV (220-nm) radiation. (a) Coarse grid structure. (b) Resolution shown by fine grid spacing.

level of spatial resolution is maintained in the streak mode. Alignment of the system was performed with a four-axis adjustable telescope mounted on the port opposing the camera system. It was estimated that the image of the 400-μm-diameter target was centered on the slit of the streak camera to an accuracy of ~40μm.

Time-Resolved Photography of Imploding Shells

Initial time-resolved photographic studies of symmetrically irradiated targets have been made with this system. These studies have permitted an evaluation of the camera and its alignment system and have provided some interesting data which can be usefully compared to the predictions of one-dimensional hydrodynamic code simulations.

The maintenance of high spatial resolution in the streak mode is illustrated in Fig. 10. This figure shows the streaked image of a 400-μm-diameter Ti sphere, irradiated uniformly with 12 beams from the OMEGA laser system. The x-ray emission (1-3 keV) persists for the duration of the laser pulse. Distinct limb-brightening of the image occurs as a consequence of the x rays originating from a thin coronal plasma surrounding the sphere. Numerical simulations and optical diagnosis of the coronal plasma under these irradiation conditions (~2×10^{14} W/cm^2) have established that the critical-density region and the ablation surface remain almost stationary throughout the pulse.[8] The curved nature of the limb-brightened image indicates the degree of pin-cushion distortion introduced by the image intensifier. This distortion can be eliminated numerically from a digitized form of the image. Alternatively, a planar proximity-focused image intensifier can be used. Fine line structure can be seen in the image, persisting for the duration of the streak record. This results from the fine mesh used in the acceleration grid of the streak tube (80 grid lines/mm) and gives an indication of the spatial resolution in the image in the streak mode.

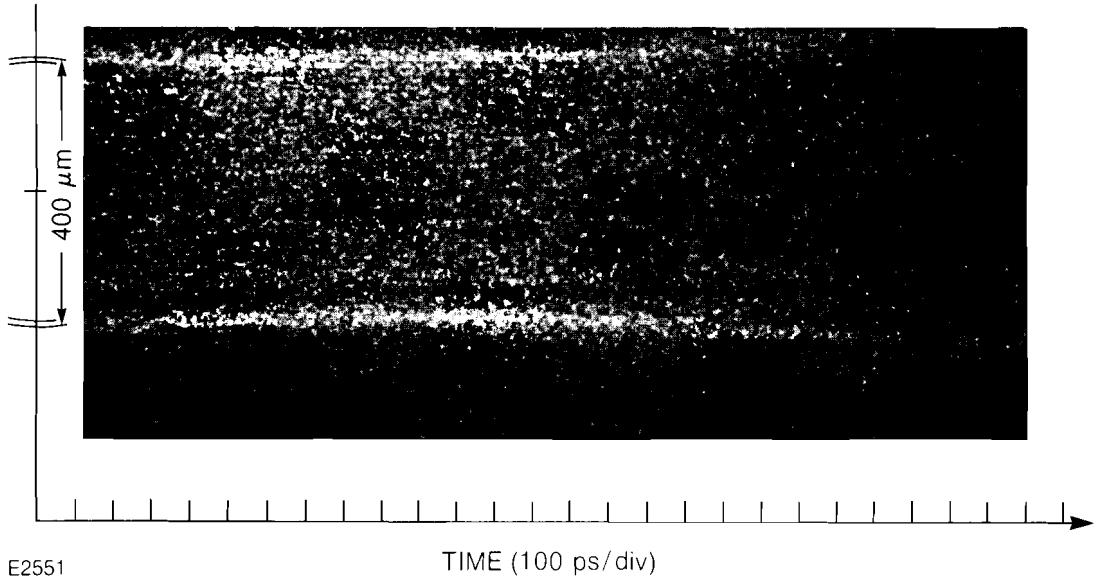

Fig. 10
Time-resolved image of the (1-3 keV) x rays emanating from a 400-μm-diameter solid Ti sphere, symmetrically irradiated by a nanosecond pulse from 12 beams of OMEGA at an intensity of 2×10^{14} W/cm².

Time-resolved images of imploding shells are shown in Fig. 11. Figure 11(a) shows the implosion of an empty 400-μm-diameter, 1.0-μm-wall, glass microballoon irradiated with 6 beams from the OMEGA system with an average intensity of $\sim1\times10^{14}$ W/cm². The x-ray image shows the symmetric compression of the shell with a maximum implosion velocity of $\sim10^7$ cm/s, with bright x-ray emission from the core of the target becoming apparent when the shell collapses on itself. The photograph shown in Fig. 11(b) is of a similarly sized target, filled with ~0.25 atm of nitrogen, irradiated at an intensity of 2×10^{14} W/cm² with a symmetric set of 12 beams of OMEGA. In this case, the initial shell radius of 200 μm is compressed with an implosion velocity above 1×10^7 cm/s, before it stagnates on the residual gas within the shell. At this point, the radius of the ablation surface is ~60 μm. Also shown in Fig. 11(b) is clear evidence of x-ray emission from within the shell. This emission occurs prior to the stagnation of the implosion and results from a shock wave, initially launched into the gas early in the implosion, impacting on the inside of the glass shell after reflection from itself at the center of the target. The continuity of the x-ray emission from this region of the target indicates that the integrity of the shell is maintained throughout the implosion. These characteristics of the implosions are in broad agreement with the predictions of one-dimensional hydrodynamic code simulations, and will be described in more detail at a later date.

Summary

We have completed the initial activation of a time-resolved x-ray imaging system to be used for photographic and shadowgraphic studies of shell implosions created by the OMEGA laser system. High temporal and spatial resolutions have been achieved and an accurate alignment system adopted. Further improvements to be incorporated

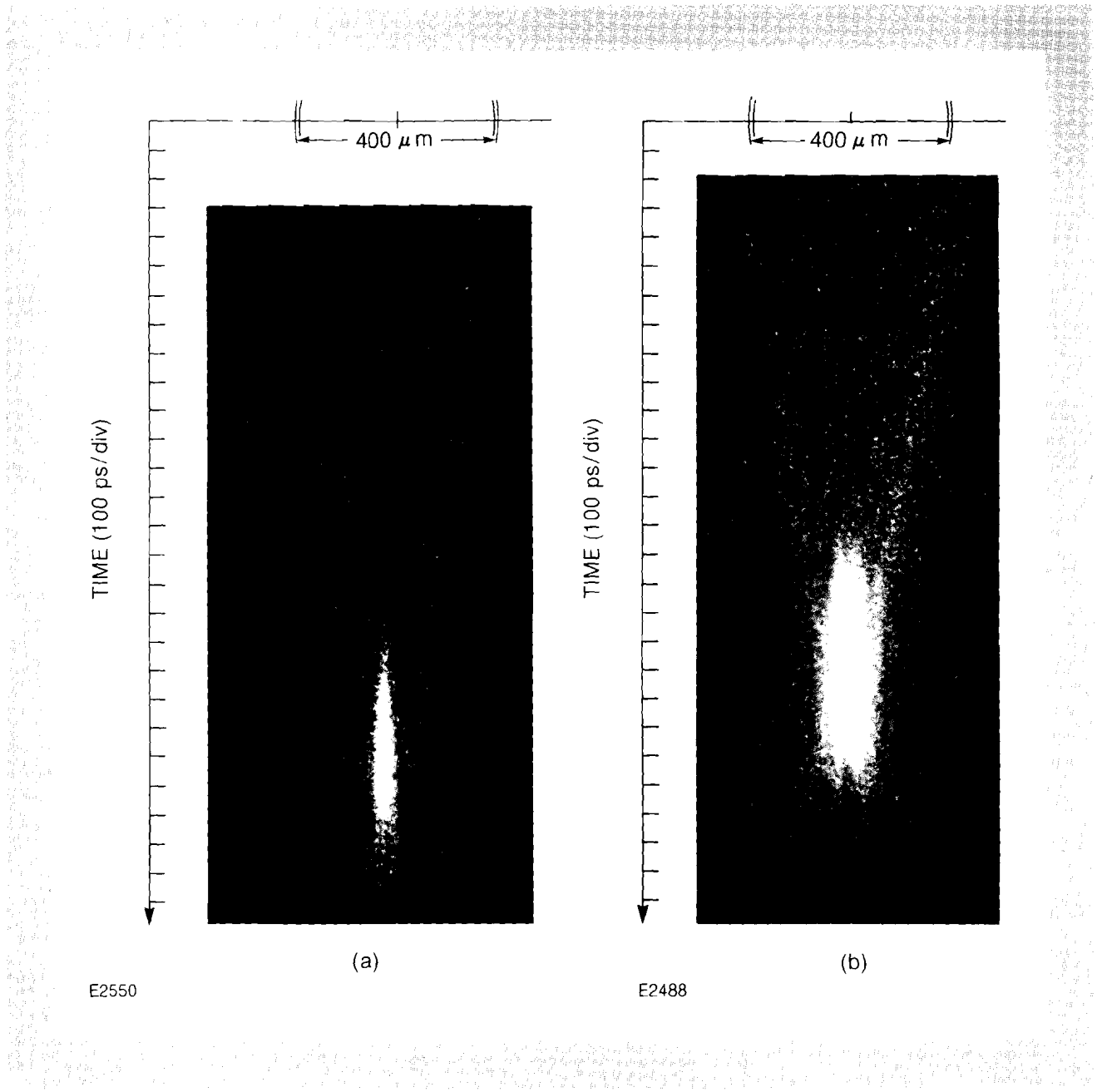

Fig. 11
Time-resolved x-ray images of (a) an empty and (b) a 0.25-atm N_2-filled glass microballoon.

into the system include the use of a proximity-focused, distortion-free image intensifier, greater x-ray spectral resolution, and the inclusion of an optical fiducial of the irradiating laser pulse. The latter will be more easily incorporated[9] for studies conducted with symmetrical arrays of up-converted 351-nm laser beams.

REFERENCES

1. D. T. Attwood, in *Proceedings of the 12th International Congress on High-Speed Photography,* edited by M. C. Richardson [*S.P.I.E.* **97**, 325 (1977)].
2. M. H. Key *et al.*, *Phys. Rev. Lett.* **41**, 1467 (1978).
3. L. W. Coleman and C. F. McConaghy, in *Proceedings of the 11th International Congress on High-Speed Photography*, edited by P. Rolls (Chapman and Hall, London, 1975), p. 196; P. R. Bird *et al.*, *ibid.*, p. 118; Yu. S. Kasyanov, A. A. Malyutin, M. C. Richardson, and V. K. Chevokin, *ibid.*, p. 561.
4. S. Letzring, Laboratory for Laser Energetics Lab Report No. 95, 1980; B. Yaakobi, D. Steel, E. Thorsos, A. Hauer, B. Perry, S. Skupsky, J. Greiger, C. M. Lee, S. Letzring, J. Rizzo, T. Mukaiyama, E. Lazarus, G. Halpern, H. Deckman, J. Delettrez, J. Soures, and R. McCrory, *Phys. Rev. A* **19**, 1247 (1979).
5. V. V. Korobkin, A. A. Malyutin, and M. Ya. Schelev, *J. Photogr. Sci.* **17**, 179 (1969).
6. M. C. Richardson, S. Skupsky, J. Kelly, L. Iwan, R. Hutchison, R. Peck, R. L. McCrory, and J. Soures, in *Proceedings of the 1983 Los Alamos Conference on Optics,* edited by R. S. McDowell and S. C. Stotlar [*S.P.I.E.* **97** (1983)].
7. P. R. Bird, D. J. Bradley, and W. Sibbett, *Proceedings of the 11th International Congress on High-Speed Photography*, edited by P. Rolls (Chapman and Hall, London, 1975), pp. 112-117.
8. M. C. Richardson *et al.*, in *Laser Interaction and Related Plasma Phenomena*, Vol. 6, edited by G. H. Miley and H. Hora (Plenum, New York, to be published 1983).
9. R. S. Marjoribanks, M. C. Richardson, J. Delettrez, S. A. Letzring, W. Seka, and D. M. Villeneuve, *Opt. Commun.* **44**, 113 (1982).

2.B Magnetic Field Effects on Electron Heat Transport

Thermal transport in laser-produced plasmas is a topic of great importance to laser fusion. In one-dimensional situations, and where moderately steep temperature gradients are believed to occur, heat fluxes considerably smaller than those predicted by the classical theories of Spitzer[1] and Braginskii[2] have been inferred experimentally. Such results are often parametrized in terms of a "flux limiter" f,[3] with the heat flux q given as a multiple f of the "free-streaming flux" q_F, defined here as $q_F = n_e kT\,(kT/m)^{1/2}$, where n_e, T, and m are the electron number density, temperature, and mass, respectively, and k is Boltzmann's constant. In two-dimensional situations, the problem is more complicated because magnetic fields generated in the laser-plasma interaction process must be considered. It is the purpose of this article to discuss some of the effects of magnetic fields on thermal transport in the presence of moderately steep temperature gradients.

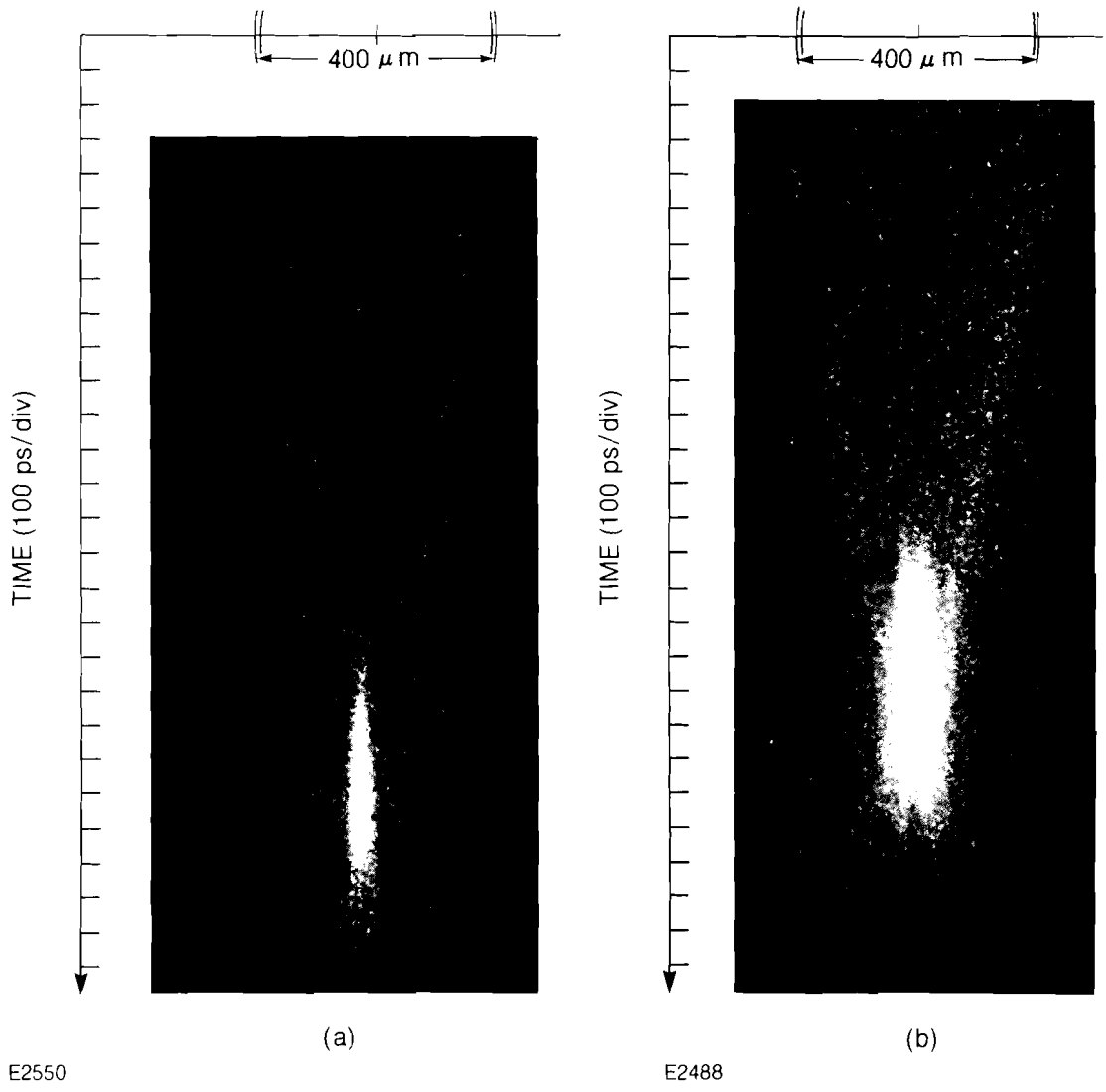

Fig. 11
Time-resolved x-ray images of (a) an empty and (b) a 0.25-atm N_2-filled glass microballoon.

into the system include the use of a proximity-focused, distortion-free image intensifier, greater x-ray spectral resolution, and the inclusion of an optical fiducial of the irradiating laser pulse. The latter will be more easily incorporated[9] for studies conducted with symmetrical arrays of up-converted 351-nm laser beams.

REFERENCES

1. D. T. Attwood, in *Proceedings of the 12th International Congress on High-Speed Photography*, edited by M. C. Richardson [*S.P.I.E.* **97**, 325 (1977)].
2. M. H. Key *et al.*, *Phys. Rev. Lett.* **41**, 1467 (1978).
3. L. W. Coleman and C. F. McConaghy, in *Proceedings of the 11th International Congress on High-Speed Photography*, edited by P. Rolls (Chapman and Hall, London, 1975), p. 196; P. R. Bird *et al.*, *ibid.*, p. 118; Yu. S. Kasyanov, A. A. Malyutin, M. C. Richardson, and V. K. Chevokin, *ibid.*, p. 561.
4. S. Letzring, Laboratory for Laser Energetics Lab Report No. 95, 1980; B. Yaakobi, D. Steel, E. Thorsos, A. Hauer, B. Perry, S. Skupsky, J. Greiger, C. M. Lee, S. Letzring, J. Rizzo, T. Mukaiyama, E. Lazarus, G. Halpern, H. Deckman, J. Delettrez, J. Soures, and R. McCrory, *Phys. Rev. A* **19**, 1247 (1979).
5. V. V. Korobkin, A. A. Malyutin, and M. Ya. Schelev, *J. Photogr. Sci.* **17**, 179 (1969).
6. M. C. Richardson, S. Skupsky, J. Kelly, L. Iwan, R. Hutchison, R. Peck, R. L. McCrory, and J. Soures, in *Proceedings of the 1983 Los Alamos Conference on Optics*, edited by R. S. McDowell and S. C. Stotlar [*S.P.I.E.* **97** (1983)].
7. P. R. Bird, D. J. Bradley, and W. Sibbett, *Proceedings of the 11th International Congress on High-Speed Photography*, edited by P. Rolls (Chapman and Hall, London, 1975), pp. 112-117.
8. M. C. Richardson *et al.*, in *Laser Interaction and Related Plasma Phenomena*, Vol. 6, edited by G. H. Miley and H. Hora (Plenum, New York, to be published 1983).
9. R. S. Marjoribanks, M. C. Richardson, J. Delettrez, S. A. Letzring, W. Seka, and D. M. Villeneuve, *Opt. Commun.* **44**, 113 (1982).

2.B Magnetic Field Effects on Electron Heat Transport

Thermal transport in laser-produced plasmas is a topic of great importance to laser fusion. In one-dimensional situations, and where moderately steep temperature gradients are believed to occur, heat fluxes considerably smaller than those predicted by the classical theories of Spitzer[1] and Braginskii[2] have been inferred experimentally. Such results are often parametrized in terms of a "flux limiter" f,[3] with the heat flux q given as a multiple f of the "free-streaming flux" q_F, defined here as $q_F = n_e kT\,(kT/m)^{1/2}$, where n_e, T, and m are the electron number density, temperature, and mass, respectively, and k is Boltzmann's constant. In two-dimensional situations, the problem is more complicated because magnetic fields generated in the laser-plasma interaction process must be considered. It is the purpose of this article to discuss some of the effects of magnetic fields on thermal transport in the presence of moderately steep temperature gradients.

Many attempts have been made to understand the physical basis of reduced heat fluxes. Three different approaches may be summarized as follows:

a) Classical theories simply do not apply in the regime of interest (thermal-electron mean free path $\lambda_T \gtrsim 0.01$ times the temperature scale length L).[4] If the electron kinetic equations are solved more accurately, the correct heat flux will result. No additional physical processes are involved. This approach has recently attracted considerable attention, particularly on account of numerical solutions of the Fokker-Planck equation, reported by Bell *et al.*,[5] which indicated reduced heat fluxes corresponding to a value of f of the order of 0.1.

b) Ion-acoustic turbulence is set up in the plasma giving rise to an enhanced electron collision frequency and therefore a reduced heat flux.[6,7]

c) Magnetic fields are generated in the plasma as a result of a lack of one-dimensional symmetry;[8] the classical theory of Braginskii[2] then predicts reduced heat fluxes due to the localization of electron orbits in the magnetic fields.

The third approach is inapplicable to ideal, one-dimensional plasmas, but real plasmas are never truly one-dimensional, whether due to the finite extent of the focal spot in single-beam experiments or to the finite level of irradiation nonuniformity in a multi-beam spherical system such as OMEGA. In CO_2-laser experiments, magnetic fields have been observed to play a significant role in enhancing collisionless lateral energy transport along the target surface and away from the focal spot.[9,10] In the more collisional plasmas produced by micron- or sub-micron-wavelength lasers, the role of magnetic fields may be important in inhibiting the inward flow of energy to the ablation region as well as in affecting the lateral smoothing of irradiation nonuniformities. In the limit of small λ_T/L, the problem of heat conduction in magnetic fields was solved by Braginskii,[2] but for moderately large λ_T/L ($\gtrsim 0.01$), a more accurate kinetic treatment is required.

A full treatment of the transport problem in moderately steep temperature gradients, including both strong and weak magnetic field limits, would require, for example, a two-dimensional Fokker-Planck treatment. To date, such treatments have been computationally prohibitive. However, it was shown by Shvarts *et al.*[11] that, in one dimension, a simple local treatment, in which the anisotropic portion of the distribution function (f_1) is bounded from above by the isotropic Maxwellian distribution function (f_0), leads to results similar in many respects to those obtained by Bell *et al.*[5] from Fokker-Planck simulations. This correspondence encourages us to extend this simple local model to two and three dimensions, including magnetic fields. While some questions will remain unanswered in the absence of a full Fokker-Planck treatment, this approach may provide some insight into the respective roles of magnetic fields and kinetic effects in inhibiting thermal conduction. In particular, we shall demonstrate that a transition occurs between flux limitation and magnetic field inhibition at moderately low values of the magnetic field.

Theory

We first review the physical basis by which electron heat transport is modified by a magnetic field, with reference to a simplified model[2] illustrated schematically in Fig. 12. The heat flux across a surface element at a given point P is obtained by summing the contributions of all electrons crossing that surface element, from all angles and from either side. Each electron transports energy characteristic of the temperature of the point at which it had its last collision; thus, in the absence of magnetic fields [Fig. 12(a)], electrons whose last collision occurred on the hotter side of the surface (H) contribute more than electrons from the other side, and the net heat flux is directed antiparallel to the temperature gradient ∇T. In the presence of a magnetic field perpendicular to the temperature gradient [Fig. 12(b)], the electron orbits are circular, and a component of heat flux perpendicular to ∇T arises. This component, which will be referred to as the "transverse" heat flux, maximizes when the average heat-carrying electron traverses half a gyrational orbit between collisions. The magnetic field also inhibits the "longitudinal" heat flux component antiparallel to ∇T [Figs. 12(c) and 12(d)], because the heat flux from the hotter side is carried by electrons whose last collision may have been at a hotter point H [Fig. 12(c)] or a colder point C [Fig. 12(d)].

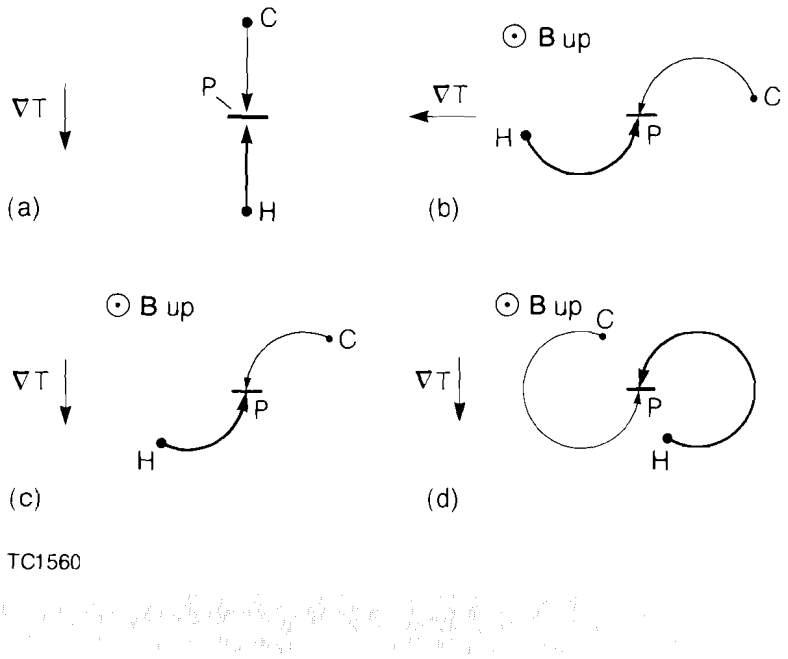

Fig. 12

*Schematic showing the effects of a magnetic field (**B**) on the orbits of heat-carrying electrons. A net flux **q**, across a surface element at a point P, occurs because electrons which had their last collision at a hotter point (H) carry more energy than electrons whose last collision occurred at a colder point (C).*

*(a) When $\mathbf{B} = 0$, **q** is directed along ∇T;*

(b) When $\mathbf{B} \neq 0$, heat can flow perpendicular to ∇T;

(c), (d) When $\mathbf{B} \neq 0$, the heat flowing antiparallel to ∇T is reduced because of averaging over electrons whose last collisions occurred at different places on the circular orbit.

The effect of the magnetic field is usually parametrized by the Hall parameter β, defined as $\omega_c \tau_{ei}$, where ω_c is the electron gyrofrequency, and τ_{ei} is the electron-ion collision time. Here, β is the number of radians traversed around a gyro-orbit between collisions; β depends strongly on the electron velocity v, since $\tau_{ei} \propto v^3$. The longitudinal heat flux associated with electrons whose β is large is greatly reduced ($\sim \beta^{-2}$), since each point on the gyro-orbit develops an equal probability of being the location of the last collision. In typical electron distribution functions, there will be some electrons with $\beta << 1$ and others with $\beta >> 1$.

Our theory starts with the Boltzmann equation for the electron distribution function f(r, v, t):

$$\frac{\partial f}{\partial t} + v \cdot \nabla f - \frac{e}{m}\left(\mathbf{E} + \frac{1}{c}\, v \times \mathbf{B}\right) \cdot \frac{\partial f}{\partial v} = C. \qquad (1)$$

E and B are the electric and magnetic fields, (-e) the electron charge, c the speed of light, and C the collision operator. We consider a coordinate system (x, y, z) with the z axis locally aligned along the magnetic field, as indicated in Fig. 13, and we use spherical polar coordinates (v, θ, ϕ) in velocity space: $v \equiv v\Omega$. We use the first two terms of a moment expansion for f:[12]

$$f(\mathbf{r}, v, t) = f_0(\mathbf{r}, v, t) + \mathbf{f}_1(\mathbf{r}, v, t) \cdot \Omega, \qquad (2)$$

where f_0 and $\mathbf{f}_1$ will be referred to as the isotropic and anisotropic components of f.

In this model, f_0 will be treated as a known function (e.g., a Maxwellian at the local temperature). The anisotropic component $\mathbf{f}_1$ is then obtained in terms of f_0 by substituting Eq. (2) into Eq. (1) and integrating Eq. (1) over $\Omega\, d\Omega$. We find:

$$\frac{\partial \mathbf{f}_1}{\partial t} + v\nabla f_0 - \frac{e}{m} E \frac{\partial f_0}{\partial v} - \omega_c \hat{z} \times \mathbf{f}_1 = \mathbf{C}_1, \qquad (3)$$

where $\omega_c = eB/mc$ is the electron gyrofrequency, and $\hat{z}$ is a unit vector in the z direction. We assume that only electron-ion Coulomb scattering contributes to the collision integral $\mathbf{C}_1$, and we use[13] $\mathbf{C}_1 = -\mathbf{f}_1/\tau_{ei}(v)$, where the velocity-dependent collision time $\tau_{ei}(v)$ is proportional to v^3. We also drop the time derivative in Eq. (3), thereby assuming a quasi-static state. Then, solving Eq. (3) for $\mathbf{f}_1$, we obtain

$$\mathbf{f}_1(v) = -\frac{\tau_{ei}}{(1+\beta^2)}\left[1 + \beta^2 \hat{z}\hat{z} \cdot + \beta\, \hat{z} \times\right]\left(v\nabla f_0 - \frac{e}{m} E \frac{\partial f_0}{\partial v}\right), \qquad (4)$$

where $\beta(v) = \omega_c \tau_{ei}(v) = \beta_0 (v/v_0)^3$, and $v_0 = (kT/m)^{1/2}$.

So far, we have followed Braginskii's treatment. Now we make use of the prescription of Shvarts *et al.*[11] We assume that the i component of Eq. (4) is satisfied for $v \leq v_i^*$, and that

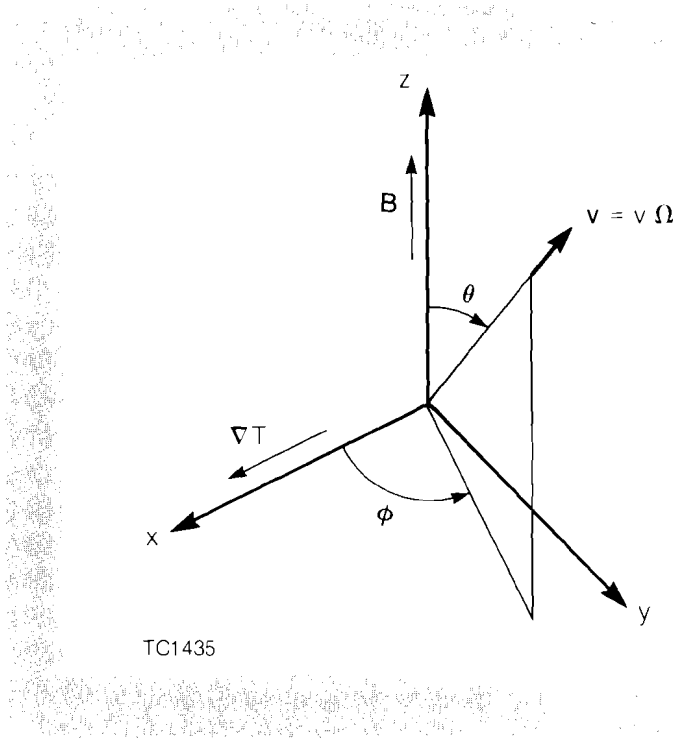

Fig. 13
Coordinate system. The z axis is taken along the magnetic field, and spherical coordinates about this axis (v, θ, φ) are used to describe velocity space. The x axis is chosen to lie along the temperature gradient. The heat flux has two components, "longitudinal" along the x axis, and "transverse" along the y axis.

$$f_{1i}(v) = \delta_i f_0(v) \tag{5}$$

for $v \geq v_i^*$, where the parameters δ_i are assigned values of order unity to ensure, at least, that the electron distribution function in Eq. (2) will never be negative. The cutoff velocities v_i^* are to be determined by iteration, and $f_{1i}(v)$ must be continuous at $v = v_i^*$. In the illustrative calculations below, we use $\delta_i = 0.67$ for each i. The detailed results will, of course, depend somewhat on the δ_i, but in view of the generally close agreement between this approach[11] and Fokker-Planck calculations[5] in one dimension, we may reasonably expect our results to yield some useful insight.

The current and heat-flux vectors are obtained by solving Eqs. (4) and (5) iteratively for the components of $\mathbf{f}_1$ and by performing the appropriate integrals over velocity space. By way of comparison, full Fokker-Planck calculations evaluate $f_0(v)$ by solving Eq. (1). Results may be obtained for a given electric field (in which case the current and heat flux are calculated), or for a given current (in which case the electric field and heat flux are calculated). Details are given in Ref. 14.

Illustrative Results

The magnetic-field-induced modifications to the heat flux are presented in terms of the Hall parameter β_0 for thermal electrons, given by

$$\beta_0 = \omega_c \tau_{ei}(v_0) = 5.10 \times 10^{21}\, BT^{3/2}/[n_e (Z+1)], \tag{6}$$

where n_e is measured in cm^{-3}, T in keV, and B in MG. (If the electron-ion momentum-transfer collision time τ_e given by Braginskii[2] had been

used in place of $\tau_{ei}(v_0)$, β_0 would be a factor of 3.8 higher.) The effect of electron-electron collisions is approximated here by using (Z+1) in place of Z, and the Coulomb logarithm is taken to be 10. For a typical plasma of Z=4 and T=1 keV, we obtain the useful relationship

$$\beta_0 \simeq (10^{21}/n_e)B, \tag{7}$$

or, at the critical density for 1-μm Nd:glass laser radiation, $\beta_0 \simeq B$, where B is in units of MG.

Magnetic fields of the order of a megagauss have been observed in the coronas of laser-fusion targets through Faraday rotation,[15] while fields of the order of 0.1 MG are harder to detect and are often considered unimportant. However, even values of β_0 as low as 0.1 are sufficient to modify the heat flux significantly, because the β corresponding to the electrons which carry the bulk of the heat is at least an order of magnitude higher.

We will restrict ourselves to the geometry of Fig. 13, with **B** aligned in the z direction and ∇T in the x direction. The current, heat flux, and electric field will all lie in the x-y plane, their longitudinal and transverse components being parallel to the x and y axes, respectively. In all cases the heat flux **q** will be expressed relative to the free-streaming flux q_F ($=n_e m v_0^3$); the ratio q/q_F may be thought of as the effective flux limiter.

In order to illustrate the main features of this model, we will consider the case where the ratio of the thermal-electron mean free path λ_I (defined as $v_T \tau_{ei}$, where $v_T = \sqrt{3}\, v_0$) to the temperature scale length L_x is relatively high (0.1), and where the current **J** is zero. (The model applies equally to the case of non-zero current, for which results are given in Ref. 14.) The normalized heat fluxes q_x/q_F and q_y/q_F are given in Fig. 14 as functions of β_0. Here, as elsewhere, the solid lines denote q_x/q_F and the dashed lines q_y/q_F, for bounded f_1. For the purposes of comparison, the thin lines denote the same quantities for unbounded f_1 (Braginskii's results[2]). The Braginskii result for $\beta_0 = 0$ (off-scale) is $q_x/q_F = 0.57$. We note that for $\beta_0 \gtrsim 0.2$, there is little difference between the bounded and unbounded results for either component. Therefore, even for a relatively small magnetic field, there is no need to invoke a flux limiter.

The asymptotic behavior of **q** at large β_0 is suggested from the form of Eq. (4): $q_x \sim \beta_0^{-2}$ and $q_y \sim \beta_0^{-1}$. From Fig. 14, it is evident that there is a strong reduction of q_x/q_F (to 0.04), even for $\beta_0 = 0.2$. At higher values of β_0 the transverse component exceeds the longitudinal component. The transverse heat flux has a peak at very low β_0 (0.03 in the Braginskii case, 0.1 in the bounded case); it should maximize when the β of heat-carrying electrons [$\sim \beta_0(v/v_0)^3$] is of the order of π, on the basis of the simple physical picture discussed earlier [see Fig. 12(b)]. Indeed, taking $\beta_0 = 0.1$ and $v/v_0 \simeq 3.2$ (see Fig. 15), we find $\beta \simeq 3$.

Figure 15 shows, plotted as functions of v/v_0, the x and y components of f_1/f_0 (upper graphs) and $(v/v_0)^5\, f_1$ (lower graphs)

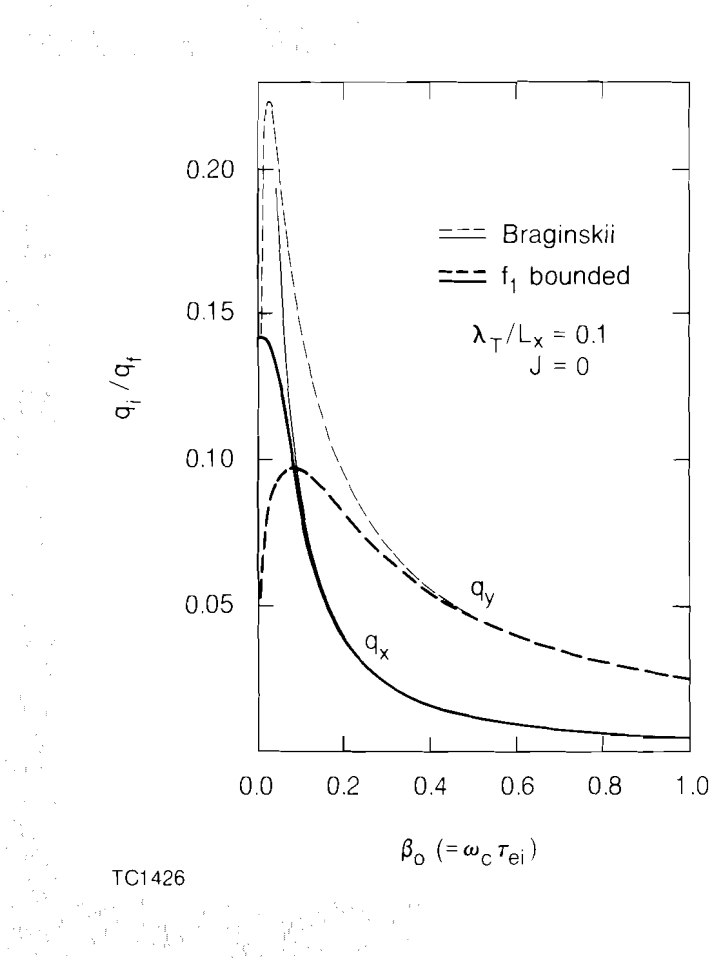

Fig. 14
Dependence of heat flux on β_0 ($=\omega_c \tau_{ei}$) for $\lambda_T/L_x = 0.1$ and zero current ($J = 0$). Solid curves, q_x; dashed curves, q_y. Light curves, Braginskii theory. Only for low values of β_0 is it necessary to modify the Braginskii theory.

corresponding to the fluxes plotted in Fig. 14, for various values of β_0. For $\beta_0 = 0$, a limit on f_{1x}/f_0 is needed to avoid large values of this ratio. No limit is needed for the higher values of β_0 shown, since the magnetic field limits f_{1x}/f_0 in the Braginskii theory, and f_{1x} is well-behaved throughout the whole velocity range. This maximum, and the minimum corresponding to the low-velocity return current, both decrease in amplitude as β_0 increases.

In our model it is always necessary to limit f_{1y}/f_0 at some velocity. For low values of β_0 (e.g., $\beta_0 = 0.2$), a strong transverse flow of high-velocity electrons is partially limited. As β_0 increases (e.g., $\beta_0 = 0.6$), the cutoff point moves to higher velocities, and the electrons which carry the bulk of the energy flow are unaffected.

The areas under the lower graphs [of $(v/v_0)^5 f_{1l}(v)$] are proportional to the heat fluxes in the respective directions. In each case, the maximum occurs at $v/v_0 \sim 3$. The integrated transverse flux is clearly greater than the longitudinal flux, and both decrease with increasing β_0.

In Fig. 16, the heat fluxes q_x/q_F and q_y/q_F are shown as functions of λ_T/L_x for various values of β_0. The classical Braginskii[2] or Spitzer-Härm[1] result for $\beta_0 = 0$ is also plotted. The Braginskii curve would of

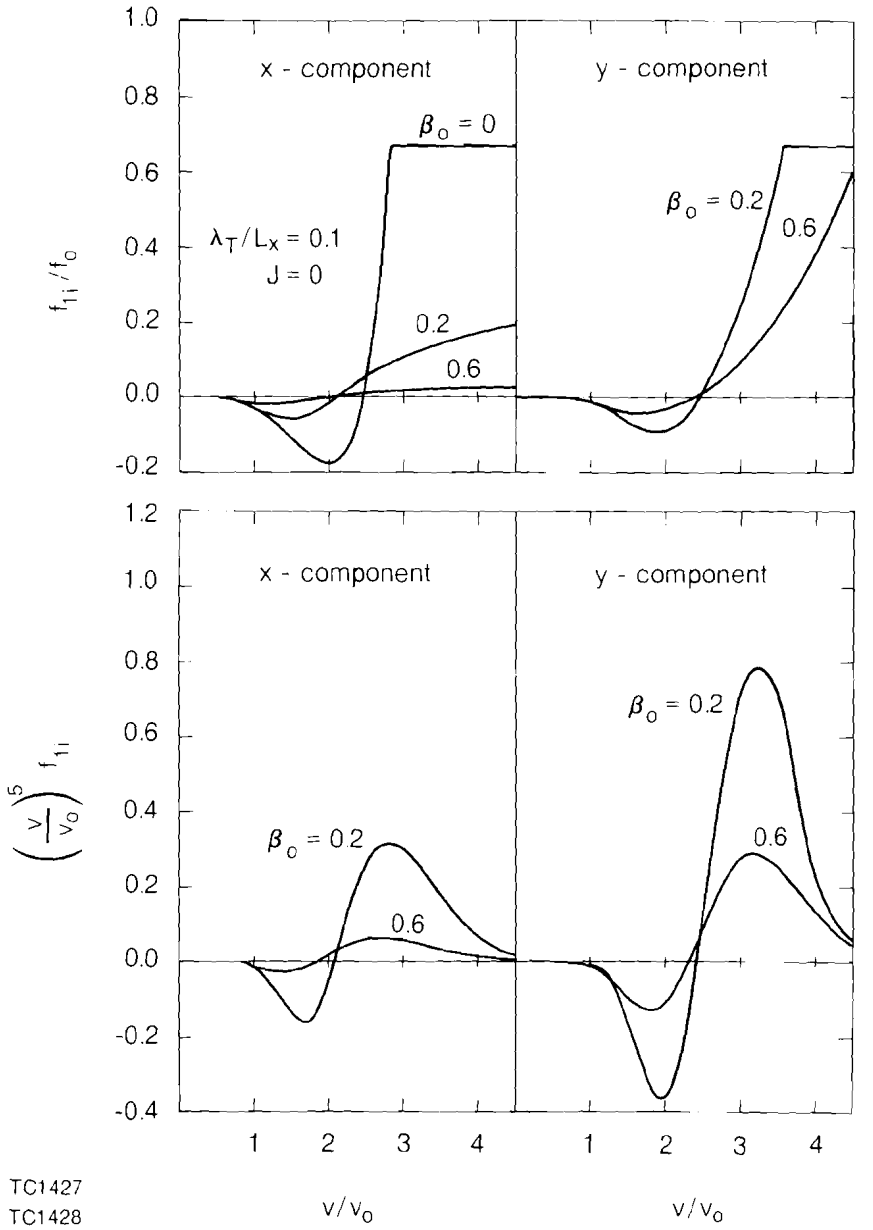

Fig. 15
Distribution functions corresponding to the fluxes plotted in Fig. 14. The upper plots, of the perturbed distribution function f_1/f_0, show that for β_0 as small as 0.2, only the transverse (y) component need be bounded. The lower plots, of the normalized heat flux $(v/v_0)^5 f_1$, show that in most cases the dominant contributions to the heat flux come from electrons with velocities $\sim 3v_0$.

course be a straight line on a linear/linear plot. There is a region in the figure ($\lambda_T/L_x \sim 0.1$, $0.1 \lesssim \beta_0 \lesssim 0.3$) where both components of the heat flux are of the order of a few percent (0.03-0.1) of the free-streaming value. This value of λ_T/L_x is typical of what may occur in laser-produced plasmas at moderately high intensities, and it is arguable that the inhibition commonly observed can be explained by very modest values of magnetic field. It must, however, be noted that the effective flux limiter implied by Fig. 16 is a strong function of both λ_T/L_x and β_0, and might lead to a greater diversity of experimentally inferred flux limiters than has been observed to date.

Figure 16 includes values of λ_T/L_x up to 1.0, but the regime of validity of this theory probably does not extend beyond $\lambda_T/L_x = 0.1$,[11] at least in the magnetic-field-free case. Beyond this limit, the heat flux is dominated by nonlocal contributions from electrons whose mean free path exceeds the temperature-gradient scale length L_x. Conversely, for smaller λ_T/L_x or for larger β_0, the nonlocal contribution decreases.

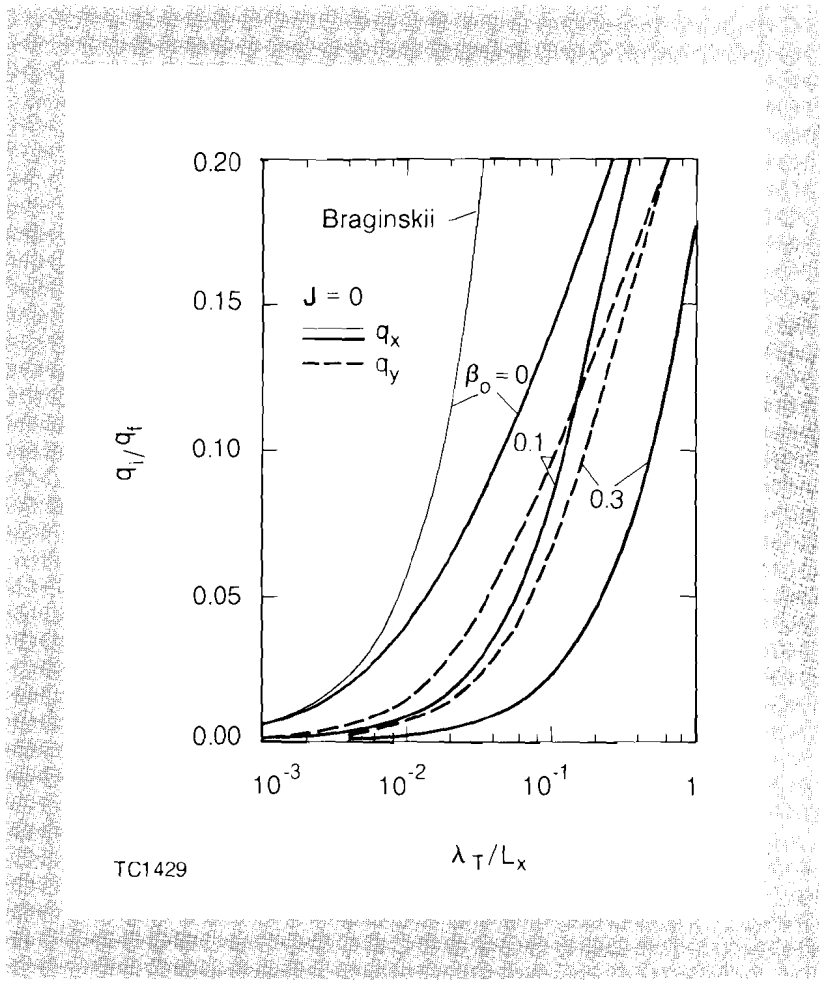

Fig. 16
Dependence of heat flux on λ_T/L_x for $J = 0$ and $\delta_x = \delta_y = 0.67$, for various β_0. Solid curves, q_x; dashed curves, q_y. Light curve: Braginskii (or Spitzer-Härm) theory for $\beta_0 = 0$. In the range $10^{-2} < \lambda_T/L_x \leq 10^{-1}$, typical of many experiments, modest magnetic fields give rise to an effective flux-limiter (q/q_f) in the range 0.01-0.1.

Summary

We have investigated the relationship between flux limiting and magnetic-field-induced transport inhibition, using a simple model which describes the transition between these two regimes in a physically reasonable way and yields some useful insight. While it would be unwise to advocate classical magnetic field inhibition as the primary explanation for the small flux limiter inferred from experiments, it is clear that these magnetic field effects deserve more careful consideration. For parameters corresponding to typical Nd:glass irradiation experiments, strong inhibition occurs for fields as small as 100 kG, an order of magnitude smaller than the megagauss fields which have been observed. At shorter wavelengths such as a third of a micron, magnetic field effects are probably less (since the collision time at the critical density scales as the square of the laser wavelength), but could still be significant.

ACKNOWLEDGMENT

This work was started at the Workshop on "The Flux-Limiter and Heat Flow Instabilities" sponsored by the Centre Européen de Calcul Atomique et Moléculaire, Université de Paris Sud, Orsay, September 1982.

REFERENCES

1. L. Spitzer and R. Härm, *Phys. Rev.* **89**, 977 (1953).
2. S. I. Braginskii, in *Reviews of Plasma Physics*, edited by M. A. Leontovich, (Consultants Bureau, New York, 1965) Vol. 1, p. 205.
3. R. C. Malone, R. L. McCrory, and R. L. Morse, *Phys. Rev. Lett.* **34**, 721 (1975).
4. D. R. Gray and J. D. Kilkenny, *Plasma Phys.* **22**, 81 (1980).
5. A. R. Bell, R. G. Evans, and D. J. Nicholas, *Phys. Rev. Lett.* **46**, 243 (1981).
6. W. M. Manheimer, *Phys. Fluids* **20**, 265 (1977).
7. D. R. Gray *et al.*, *Phys. Rev. Lett.* **39**, 1270 (1977).
8. J. A. Stamper *et al.*, *Phys. Rev. Lett.* **26**, 1012 (1971).
9. D. W. Forslund and J. U. Brackbill, *Phys. Rev. Lett.* **48**, 1614 (1982).
10. M. A. Yates *et al.*, *Phys. Rev. Lett.* **49**, 1702 (1982).
11. D. Shvarts, J. Delettrez, R. L. McCrory, and C. P. Verdon, *Phys. Rev. Lett.* **47**, 247 (1981).
12. I. P. Shkarofsky, T. W. Johnston, and M. P. Bachynski, *The Particle Kinetics of Plasmas* (Addison-Wesley, Reading, Massachusetts, 1966).
13. I. P. Shkarofsky, *Phys. Rev. Lett.* **42**, 1342 (1979).
14. M. Strauss, G. Hazak, D. Shvarts, and R. S. Craxton, in Proceedings of the CECAM Workshop on "The Flux Limiter and Heat Flow Instabilities," Paris, 1982 (unpublished).
15. J. A. Stamper and B. H. Ripin, *Phys. Rev. Lett.* **34** , 138 (1975); J. A. Stamper, E. A. McLean, and B. H. Ripin, *ibid.* **40**, 1177 (1978); A. Raven, O. Willi, and P. T. Rumsby, *ibid.* **41**, 554 (1978).

2.C Statistical Ray Tracing in Plasmas with Random Density Fluctuations

Statistical ray tracing is a method of describing the random behavior of light rays in a plasma in terms of the statistical properties of the random electron density component. As in the earliest random-medium propagation formalisms, this method is based on the use of geometrical optics to sample the random density fluctuations with light rays.[1-3]

The random-walk spreading of beams of light due to random density fluctuations is of interest to laser fusion because spreading reduces small-scale illumination nonuniformities and because the efficiencies of various energy absorption mechanisms lose some of their angle-of-incidence dependence as the beam acquires a wider angular distribution. Such considerations could affect target illumination uniformity, which is a crucial quality factor in the success of high-compression implosions.[4] The results of virtually any laser-plasma interaction experiment where properties of reflected or transmitted light are being measured are bound to be affected at some level by random density fluctuations. The use of the spreading of transmitted or reflected laser beams as a corona-structure diagnostic is not without precedent; Chandrasekhar[1] was among the first to use the random motion and scintillation of stellar images to obtain estimates of the relevant scale lengths and density fluctuation amplitudes of the turbulent atmospheric layer causing this behavior.

The theory of wave propagation in random media has advanced beyond the geometrical-optics formalisms[2,3] and has been applied to ionospheric scattering[5] and marine acoustics.[6] Even though our immediate concern is laser fusion, it should be noted that the work to be described in this article is potentially applicable to wave propagation in random media in other physical contexts.

An important result of our work has been the extension of statistical ray-tracing techniques to problems where the non-random "background" density component is inhomogeneous. It has been found that a strongly refracted beam of light will not only spread due to the random density fluctuations; its mean (center) ray will also drift slightly from the path taken by the unperturbed, zero-fluctuation ray path. To our knowledge, such a drift has never been derived or described in a statistical ray-tracing theory, but it is a necessary part of a quantitatively complete beam-propagation theory. A drift term has been formally expressed in a wave diffusion theory by Carnevale *et al.*, but this term was not evaluated for circumstances general enough to give a nonzero result for this effect.[7]

The calculation of energy absorption efficiencies in the presence of density fluctuations superimposed upon an idealized density profile has been considered elsewhere for coherent disturbances of the density profile[8] and for random density fluctuations confined to restricted regions along density gradients near the critical surface where resonance absorption occurs.[9,10] The formalism to be discussed here deals more directly with the propagation of the light and considers random density fluctuations throughout the plasma, so that the results depend upon the statistical properties of the plasma as a whole, rather than on a restricted class of coherent density ripples or on fluctuations in a restricted region.

To demonstrate the use and validity of statistical ray-tracing, results for the evolution of intensity profiles of beams incident on a plane-parallel linear-profile plasma will be presented and compared with numerical Monte-Carlo results.

The statistical-ray-tracing approach is applicable only to problems where the electron-density profile can be decomposed into a non-fluctuating component and a random component that gives each ray in a beam of light a random perturbation. In hydrodynamic simulation codes, the light intensity distribution is often computed by tracing an ensemble of rays, ray by ray, through the plasma. The electron-density information from such codes does not include an identification of random and non-fluctuating components, but the statistical-ray-tracing method could be useful if such a decomposition could be postulated *ad hoc*. For example, one could model the effects of fluctuations whose scale lengths are too short to be resolved by a computational fluid mesh. In the illustrative example to be considered below, the non-fluctuating, unperturbed density component is represented by an idealized analytic form. This allows the intensity profile of a beam of light to be expressed in terms of the solution of a set of coupled ordinary differential equations. This simplification makes it relatively easy to study the dependence of the evolution of a beam on the statistical parameters of the density fluctuations; a much greater effort would be required to obtain a large data base from Monte-Carlo calculations.

Statistical Ray-Tracing Theory

To calculate the behavior of a statistical ensemble of perturbed ray trajectories, one begins with the geometrical optics ray equation[11]

$$\mu \frac{d}{ds} \mathbf{v} = \nabla\mu - \mathbf{v}(\mathbf{v} \cdot \nabla\mu), \tag{1a}$$

$$\mu = (1 - n_e/n_c)^{1/2} \tag{1b}$$

for the deflection of the ray direction vector $\mathbf{v}$ at a point along the ray trajectory specified by the path-length parameter s. The index of refraction μ is given here in terms of the electron density n_e and the critical electron density n_c. The ray equation relates ray-trajectory perturbations to zero-mean density perturbations δn superimposed upon a background density n_o, where

$$n_e = n_o + \delta n, \tag{2a}$$

and

$$\langle \delta n \rangle = 0. \tag{2b}$$

The brackets here denote a local average. This perturbation approach requires that the rms amplitude of the density fluctuations, σ, be small so that the relative fluctuations of the index of refraction are small. This condition is simply

$$\sigma \ll n_c - n_o, \quad \text{or} \quad \delta\mu/\mu \ll 1, \tag{3a}$$

where

$$\sigma^2 = \langle \delta n^2 \rangle. \tag{3b}$$

The density fluctuations are characterized by a correlation length h that must be much smaller than the overall scale length L of the problem. For the present, a suitable example is

$$\langle \delta n\,(\mathbf{x})\ \delta n\,(\mathbf{x}+\Delta\mathbf{x})\rangle$$

$$= \sigma(\mathbf{x})\ \sigma(\mathbf{x}+\Delta\mathbf{x})\ \exp\left(-\Delta\mathbf{x}\cdot\Delta\mathbf{x}/h^2\right), \tag{4a}$$

where

$$h \ll L \sim n_0/|\nabla n_0| \sim \sigma^2/|\nabla\sigma^2|. \tag{4b}$$

This example contains a long-scale-length spatial dependence in addition to the short-scale-length Gaussian cutoff.

By passing a sequence of rays from a pencil beam through a large sample of these fluctuations, the following equation for the mean-ray direction vector $\langle \mathbf{v}\rangle$ is obtained:

$$\frac{d}{ds}\langle \mathbf{v}\rangle = -\frac{[\nabla n_0 - \mathbf{v}\,(\mathbf{v}\cdot\nabla n_0)]}{2\,(n_c - n_0)}$$

$$+\frac{[\nabla\sigma^2 - \mathbf{v}\,(\mathbf{v}\cdot\nabla\sigma^2)]}{8(n_c - n_0)^2} - \frac{\pi}{2}\,\frac{\sigma^2}{h(n_c - n_0)^2}\,\mathbf{v}. \tag{5}$$

Each ray has the same initial direction vector v. Equation (5) is obtained by integrating Eq. (1a) over a path interval that is small in comparison with the overall scale length of the problem, yet long enough in comparison with the correlation length, so that the non-accumulating effects of the fluctuations average out. In obtaining Eq. (5), Eqs. (1) and (2) must be iterated at least once for the lowest-order nonzero fluctuation effects to appear.

The first term in Eq. (5) represents the refraction of the rays due to the unperturbed density gradient. The second term represents an additional drift due to the gradient of the fluctuation amplitude, and the third term represents the foreshortening of the mean direction vector due to the spreading of the individual rays away from the mean direction. The net shift and spreading occur because correlations in the density fluctuations cause the random impulses to fortuitously reinforce each other. It is significant that no drift effect due to the simultaneous presence of density fluctuations and a nonzero background gradient is found. The slowing term due to the spreading of the beam agrees with the earliest results in ray statistics.[1,2]

The angular spreading rate of the light beam is obtained by solving Eq. (1a) to lowest order in δn and forming the ensemble average of the square of the ray deflections. This gives

$$\frac{d}{ds}\langle \mathbf{v}_\perp\cdot\mathbf{v}_\perp\rangle = \pi^{1/2}\,\frac{\sigma^2}{h(n_c - n_0)^2}\ , \tag{6}$$

which is the growth rate of the mean-square angular radius of the ray distribution. The growth rate is just what one would expect for a random walk in the profile plane where each ray receives a random angular displacement of roughly $\sigma/(n_c-n_o)$ radians from each independent fluctuation it traverses, or, equivalently, once per correlation length h along its path. The total rms angular displacement is essentially the displacement due to one impulse, or one fluctuation, multiplied by the square root of the number of impulses, just as is indicated by the form of Eq. (6).

Solving an Illustrative Problem

The problem to be considered below is that of a beam spreading as it refracts through a plane-parallel uniform-gradient plasma. The solution is cast in the form of an elliptical Gaussian ray distribution in the profile plane of the beam. This plane is represented in Fig. 17 by the X-Y axes placed normal to the trajectory of the mean ray, $\mathbf{x}$ (s), at the point denoted by s. The unperturbed trajectory $\mathbf{x}_o(s)$ is assumed to be known from the solution to this problem for $\sigma=0$. The displacement of the mean ray from the unperturbed trajectory can be found by integrating the beam shift term in Eq. (5). The beam profile distribution is centered on the mean ray and is represented in Fig. 17 by an isointensity surface, such as the rms beam-radius surface. The evolution equation for this distribution is calculated by propagating each infinitesimal phase-space element of the distribution an infinitesimal distance while allowing each element to broaden at the rate given by Eq. (6). The evolution equation itself and the details of its derivation and solution will be presented elsewhere. The beam-profile intensity distribution can be written in terms of the profile-plane phase space $(\mathbf{X}_\perp, \mathbf{V}_\perp)$ in the form

$$f(\mathbf{X}_\perp, \mathbf{V}_\perp) \propto \exp\left\{-\left[\frac{X^2}{a_x(s)} + \frac{2XV_x}{b_x(s)} + \frac{V_x^2}{c_x(s)}\right]\right.$$

$$\left. -\left[\frac{Y^2}{a_y(s)} + \frac{2YV_y}{b_y(s)} + \frac{V_y^2}{c_y(s)}\right]\right\}, \qquad (7)$$

where either of the principal (X or Y) axes remains in a plane parallel to the constant-density surfaces of the unperturbed plasma as the refraction of the mean beam rotates the profile plane. The evolution equation for f reduces to a set of coupled ordinary differential equations for the six parameters in Eq. (7), $a_x(s)$, $a_y(s)$, etc. For cases without the high degree of symmetry of the plane-parallel problem, more parameters may be needed.

Statistical and Monte-Carlo Results for the Illustrative Problem

The plane-parallel plasma considered here is illustrated in Fig. 18 with superimposed isodensity contours for typical density fluctuations with constant rms amplitudes of 4% and 1% of the critical density. Density fluctuations such as these are generated for the Monte-Carlo

solutions to this problem. These fluctuations are expressed within the Monte-Carlo calculation as a Fourier series with component amplitudes set according to the discrete spectrum needed to give the correlation function in Eq. (4a) and with phases taken from a random-number generator. The Fourier components in frequency space are chosen such that the fluctuations and the correlation function are periodic in space with the period chosen to be equal to one scale length L. The electron density can be written as

$$n_e = (x/L)n_c + \delta n(x, y, z). \tag{8}$$

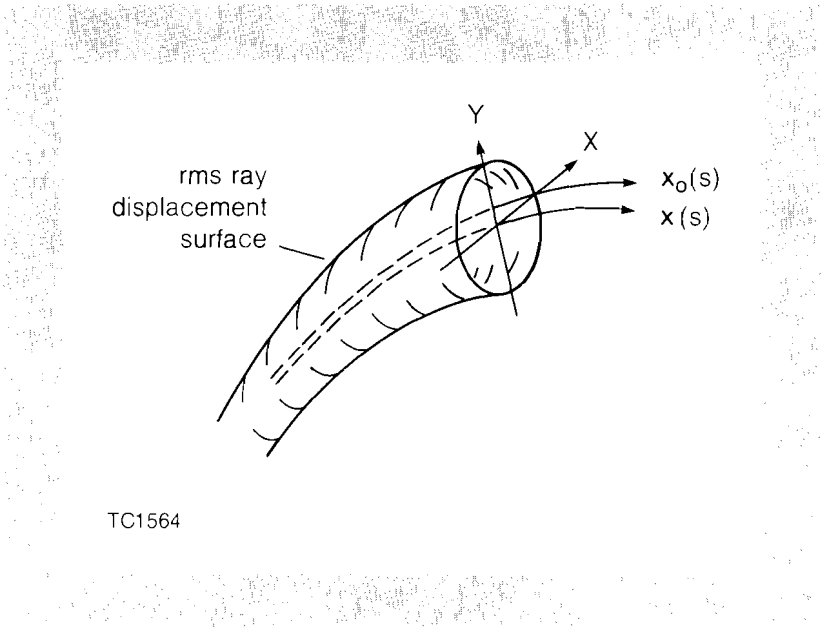

Fig. 17
*A statistical description of a light beam consists of an intensity distribution in the phase space transverse to the mean ray trajectory, **x**(s), at a point specified by the path-length parameter s. The mean ray is generally shifted from the path of the unperturbed ray, $\mathbf{x}_o(s)$. The beam envelope, defined by the rms displacement of rays from the mean ray along any direction in the profile plane, provides a concrete visualization of the beam.*

The correlation length in this example is chosen to be h/L = 0.1. Each frame in Fig. 18 shows how a typical ray wanders from the unperturbed path due to these fluctuations.

Figure 19 shows how 49 different rays propagate through these same two plasmas. For each ray, the phases of the fluctuation Fourier components are changed. The rms spatial widths of these beams calculated according to the statistical-ray-tracing method can be used to construct the rms beam envelope. The boundaries of this envelope in the plane of refraction of the unperturbed ray are drawn in Fig. 20 so that Figs. 19 and 20 can be compared by superposition. Most of the Monte-Carlo rays lie within the rms boundaries. It is interesting to note that qualitative features, such as the focusing of the beam just after

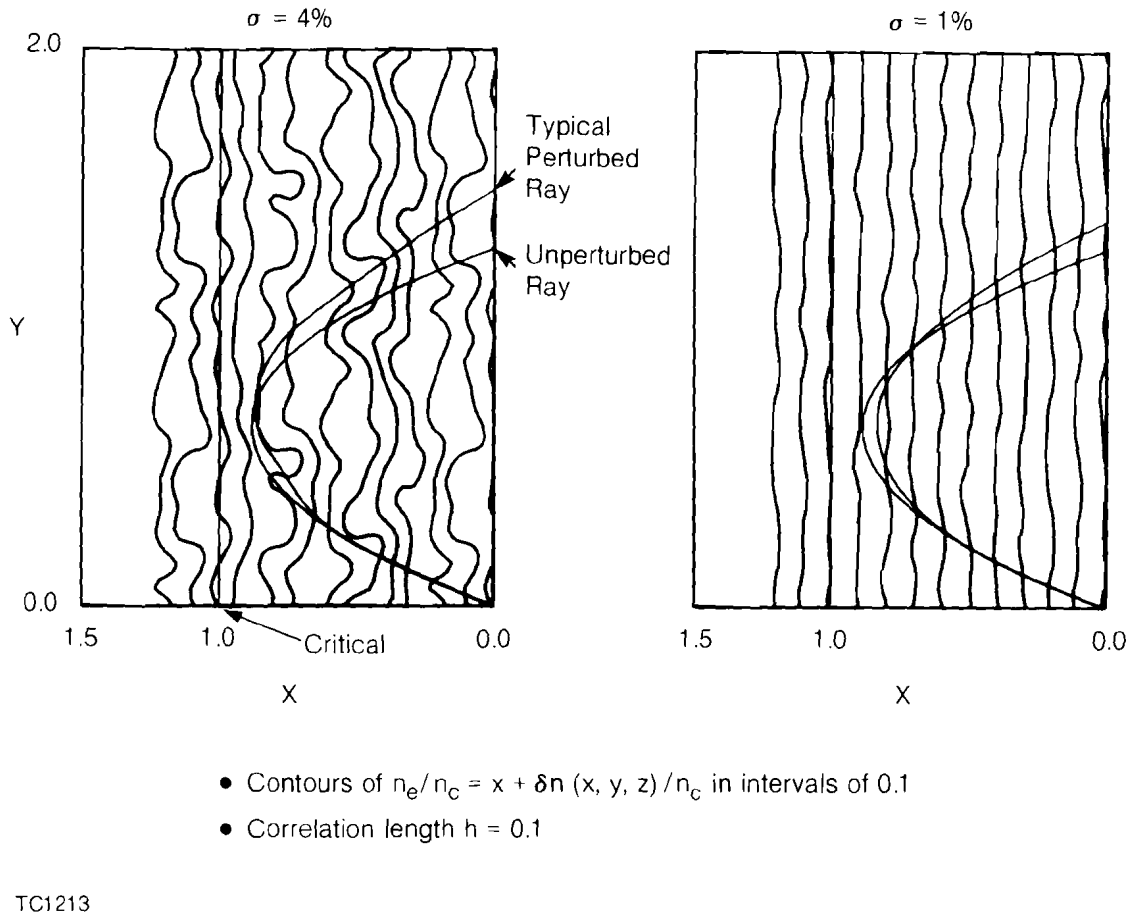

Fig. 18
Plane-paralliel uniform-gradient plasmas with superimposed density fluctuations indicated by isodensity contours. Cases with rms fluctuation amplitudes of $\sigma/n_c = 0.01$ and 0.04 are shown. The correlation length h is chosen to be h/L = 0.1. Each frame shows how a typical ray wanders from the unperturbed path due to the given fluctuations.

the turning point, are reproduced. This focusing by the background density gradient gives the beam an elliptical profile.

A more quantitative comparison of the Monte-Carlo and statistical methods is shown in Fig. 21 where the rms angular radii (at the point of emerging from the plasma) are plotted as functions of the angle of incidence. The emerging beam profile is elliptical with principal axes in and normal to the unperturbed plane of refraction. Here, $\sigma/n_c = 0.01$ and h/L = 0.1. The scatter of the Monte-Carlo points is due to the limited number (27) of trials taken per run. The agreement of these

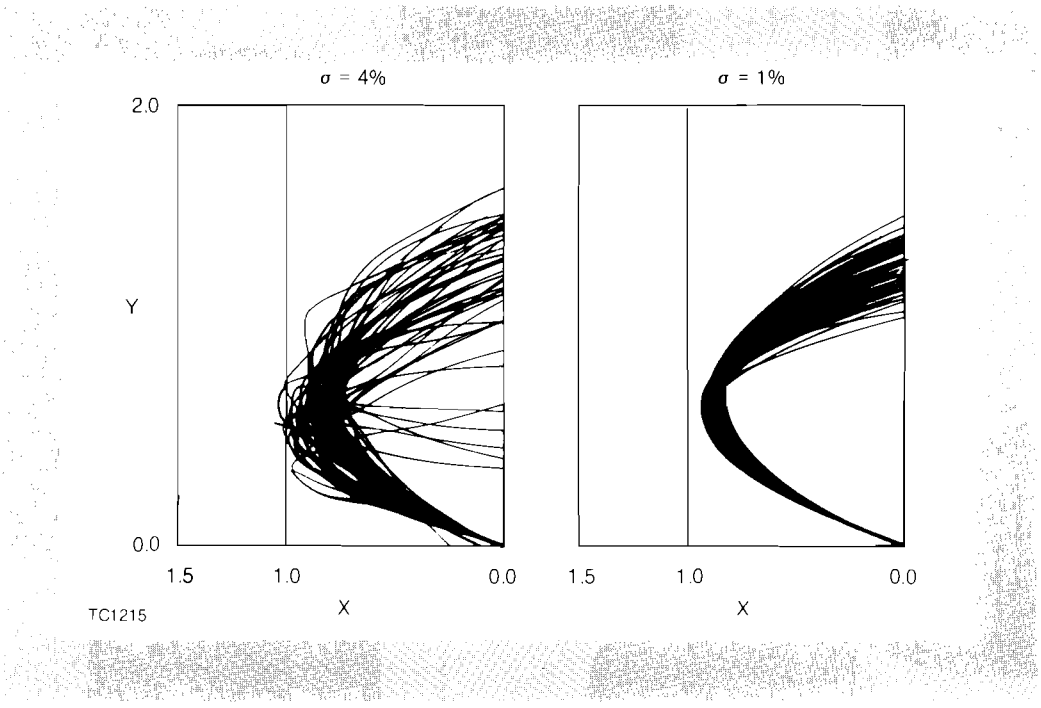

Fig. 19
Bundles of 49 rays propagating in the same conditions illustrated in Fig. 18. Each ray shown propagates according to a statistically independent sample of the fluctuation distribution. The bundles are Monte-Carlo representations of a spreading beam.

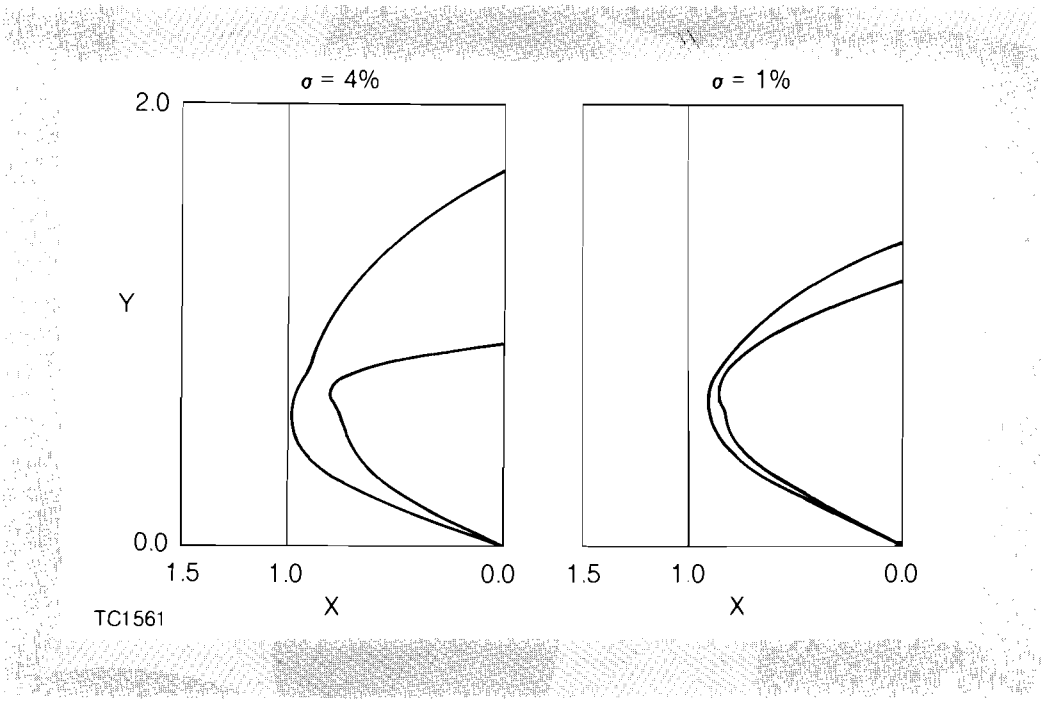

Fig. 20
The outlines of the rms ray-displacement envelopes obtained from the statistical ray-tracing theory for the same conditions as in Figs. 18 and 19. The agreement between the statistical and Monte-Carlo calculations is apparent from the superposition of the corresponding frames of this figure and Fig. 19.

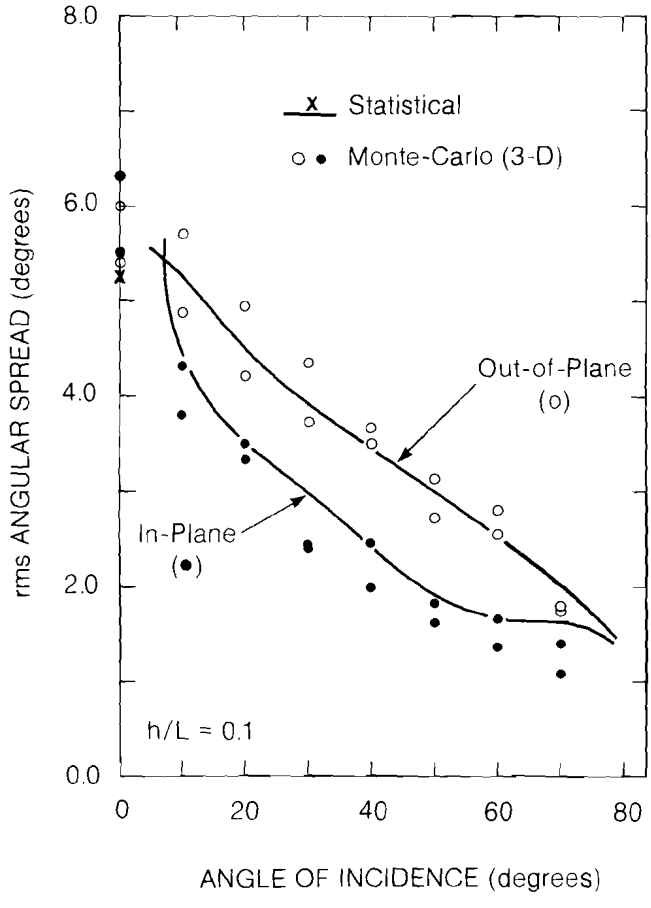

Fig. 21
The principal rms angular radii of the elliptical profile of the beam (at the point where it emerges from the slab) is plotted as a function of the angle of incidence of the initial pencil beam. The conditions $\sigma/n_c = 0.01$ and $h/l = 0.1$ are assumed. The statistical ray-tracing results fall within the scatter of the dots representing Monte-Carlo calculations.

points with the statistical theory curves is well within this scatter. The spatial width of the emerging beam obtained by both methods is plotted in Fig. 22, where the agreement between the statistical curve and the scattered Monte-Carlo points is also apparent. The isolated "X" in both Figs. 21 and 22 represents a statistical result for the singular normal-incidence case. As the initial beam approaches normal incidence, the distance of closest approach to the critical surface of the unperturbed ray path becomes smaller, and the small-perturbation condition, Eq. (3a), is eventually violated. The calculation of the isolated normal-incidence point avoids this difficulty by simply neglecting any beam spreading that occurs within one correlation length of the unperturbed critical surface. This *ad hoc* "fix-up" affects only a small fraction of the total ray path, so it is not unreasonable that the result should be in rough agreement with the Monte-Carlo results.

According to the σ-scaling of the angular spreading rate given by Eq. (6), the angular and spatial widths given in Figs. 21 and 22 should scale linearly with σ. This scaling is verified in Fig. 23 for the spatial

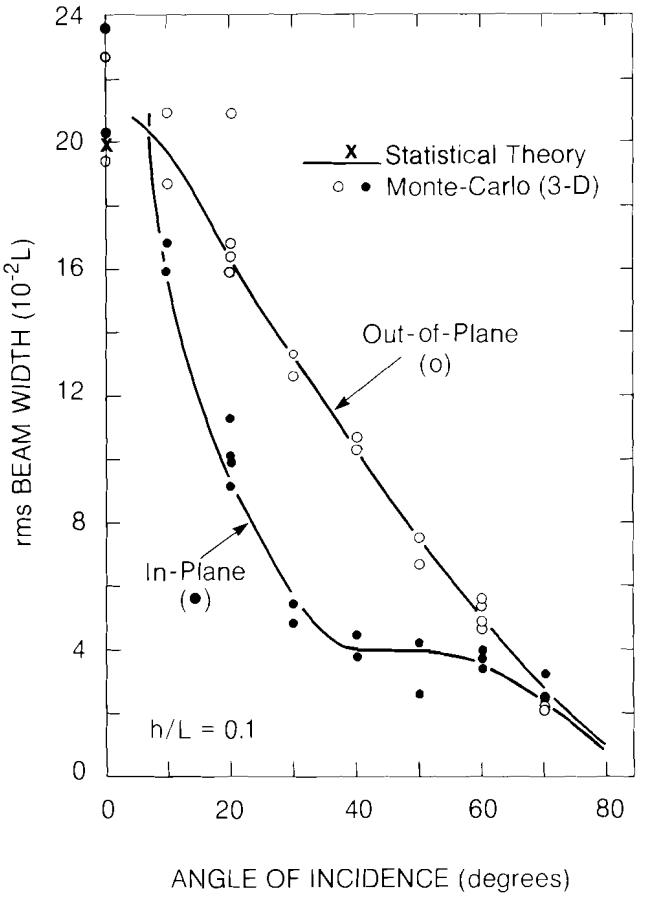

Fig. 22
Same as Fig. 21, except that the principal rms spatial radii, rather than angular radii, are plotted.

beam width in the plane of refraction for an angle of incidence of 20°. The Monte-Carlo runs verify this linear scaling up to a fluctuation level of $\sigma/n_c \sim 0.1$. At the point along the unperturbed ray most closely approaching the critical surface, density fluctuations of this magnitude typically give index-of-refraction fluctuations comparable to the unperturbed index of refraction, which violates the small-perturbation condition, Eq. (3b). The verification of linear scaling for such large fluctuation amplitudes is a strong indication of the reliability of the statistical method.

It has been observed experimentally that angle-of-incidence dependences of energy absorption efficiencies are weaker than predicted by simple analytical models.[9] In some cases, such an effect may be attributable to density fluctuations. Figure 24 shows the absorption fraction for inverse bremsstrahlung for the plane-parallel, uniform-gradient plasma considered above, plotted as a function of the angle of incidence. The circles represent individual two-dimensional Monte-Carlo calculations for $\sigma/n_c = 0.05$ and $h/L = 0.1$. These are to

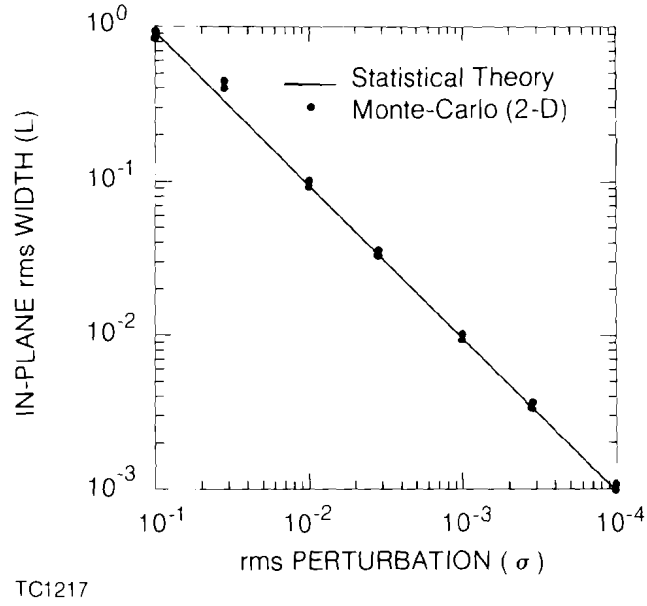

Fig. 23
The rms width, in the unperturbed plane of refraction, of the emerging beam plotted as a function of the rms density-fluctuation amplitude for an angle of incidence of 20° and for $h/L=0.1$. The predicted linear scaling of the beam width with the fluctuation amplitude is verified by Monte-Carlo calculations, up to a fluctuation level of $\sigma/n_c=0.1$.

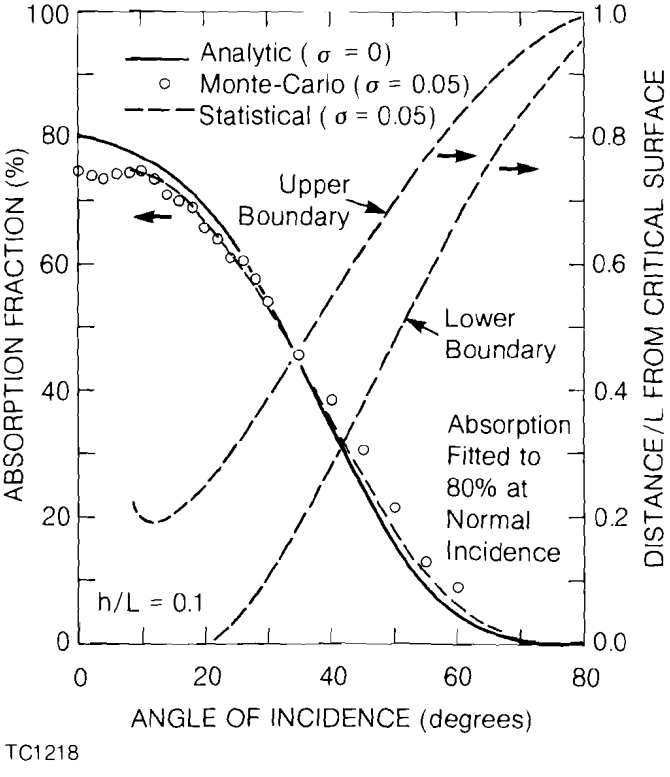

Fig. 24
Monte-Carlo (circles) and statistical ray-tracing (dashed curve) estimates of the inverse-bremsstrahlung absorption fraction are plotted (left-hand scale) as functions of the angle of incidence for the σ/n_c = 0.05, h/L = 0.1 case. The absorption coefficient is chosen to give 80% absorption at normal incidence for the σ = 0 result shown by the solid curve. The statistical estimate of the absorption is obtained using penetration-depth distribution results represented by the upper-boundary and lower-boundary curves (right-hand scale).

be compared with the solid curve obtained analytically for the $\sigma = 0$ case.[12] In these calculations, the absorption coefficient was set such that 80% absorption would be obtained for normal incidence with $\sigma = 0$. The pair of dashed curves, read with the right-hand scale, gives the statistical theory results for the upper and lower rms beam boundaries at the point of closest approach to the critical surface, as a function of angle of incidence. The leveling of the Monte-Carlo angular dependence occurs at angles of incidence below about 15°, roughly where the statistical theory predicts a significant concentration of rays grazing the critical surface, a region accessible only to normally incident rays in an unperturbed plasma. Further decreases in the angle of incidence do not increase the concentration of near-critical rays significantly, just as if the beam were incident on the unperturbed plasma with an initial angular radius of about 15°.

The dashed absorption curve in Fig. 24 is a simple statistical-theory estimate of the change in the absorption efficiency due to the given fluctuations. Since the inverse-bremsstrahlung absorption cross section increases rapidly with electron density, it is assumed that the energy absorbed from a ray is most strongly dependent on the maximum penetration depth and less sensitive to the shape of the path, as long as the perturbed paths remain reasonably smooth. The statistical estimate is obtained by convolving the analytical zero-fluctuation result with a penetration depth distribution obtained from the statistical calculations. As can be seen in Fig. 24, this statistical estimate gives results similar to the Monte-Carlo results. The crudeness of the quantitative agreement is not unexpected, given the simplicity of the estimate. Nevertheless, both the statistical and Monte-Carlo calculations give curves that cross the zero-fluctuation result near a 35° angle of incidence, and the distinct flattening of the angle-of-incidence dependence of the statistical results occurs very near where Monte-Carlo results suggest. Closer agreement would certainly be obtained by making fuller use of the statistical ray distribution over the entire path of the spreading beam. This has yet to be done. It should be emphasized, however, that the statistical absorption-efficiency results are encouraging as examples of what can be obtained using relatively simple estimates, without resorting to lengthy Monte-Carlo calculations.

Summary

The most significant result of this work is the application of statistical ray-tracing techniques to strongly refracting plasmas. The agreement obtained between the statistical and Monte-Carlo methods verify the reliability of the statistical results. It should be noted that density fluctuations as small as a few percent of the critical density with about ten correlation lengths per scale length can result in angular spreads in reflected beams of the order of 10°. The statistical method offers a means to obtain estimates of density fluctuation effects that are otherwise obtainable only by time-consuming Monte-Carlo methods. Finally, although we have concentrated on laser-fusion applications, it should be stressed that theories of wave propagation in random media are of general applicability. The work we have presented is potentially applicable to a number of other areas.

REFERENCES

1. S. Chandrasekhar, *Mon. Not. R. Astron. Soc.* **112**, 475 (1952).
2. L. A. Chernov, *Wave Propagation in a Random Medium* (Dover, New York, 1960).
3. V. I. Tatarski, *Wave Propagation in a Turbulent Medium* (Dover, New York, 1961).
4. LLE Review **12**, 5 (1982).
5. F. Villars and V. F. Weisskopf, *Phys. Rev.* **94**, 232 (1954).
6. *Sound Transmission through a Fluctuating Ocean*, edited by S. M. Flatté (Cambridge University Press, Cambridge, 1979).
7. M. Carnevale, B. Crosignani, and P. DiPorto, *Phys. Rev. Lett.* **49**, 916 (1982).
8. A. Montes and M. Hubbard, *Plasma Phys.* **21**, 885 (1979).
9. J. J. Thompson *et al.*, *Phys. Fluids* **21**, 707 (1978).
10. R. Draglia, *Phys. Fluids* **20**, 1682 (1983).
11. L. D. Landau and E. M. Lifshitz, *Electrodynamics of Continuous Media* (Pergamon, New York, 1960), §65.
12. J. W. Shearer, *Phys. Fluids* **14**, 183 (1971).

2.D Automated Control and Monitoring of Ablation-Layer Coating

The ablation layer of a laser-fusion target is the outer coating, typically composed of a low-Z material where the laser energy is absorbed. Heat from the absorbed laser energy causes the material in the absorption region to expand radially outward; this results, by conservation of momentum, in the implosion of the inner layers of the target. At LLE, ablation layers composed of a hydrocarbon polymer, parylene (poly-para-xylylene),[1] have been deposited on microballoon targets[2] of high degrees of smoothness and uniformity.[3]

The necessity of developing the automated ablation-layer deposition system now in use resulted primarily from the fact that the manual process was excessively time-consuming. The manual process required the continuous attention of an operator, usually for several hours per target. In addition, the coating thickness of any given target could not be controlled to within the precision required for certain experiments. An operator, with skill and practice, could obtain the desired coating thickness to within an accuracy of only 10 to 15%. The automated system operates virtually unattended, and with the new thickness monitoring system in place, the deposition process can be stopped precisely enough to control final thicknesses to within 10 nm. This tolerance is typical of those required for thermal transport experiments on the OMEGA system, where thermal electron conduction through precisely known thicknesses of ablation-layer material was measured.[4]

The parylene deposition process consists of the three steps illustrated in Fig. 25: (1) vacuum sublimation at elevated temperature of a stable crystalline dimer, 2,2-paracyclophane; (2) the pyrolysis at high temperature of the dimer to form p-quinodimethane; and (3) simultaneous deposition and polymerization of the p-quinodimethane to form parylene. Sublimation usually occurs at 100-200°C, pyrolysis at 650°C, and deposition at room temperature. By carefully controlling the deposition process, very smooth and uniform conformal coatings can be deposited on microballoon laser-fusion targets. Additional technical details for this process were reported in LLE Review, Volume 9.[3]

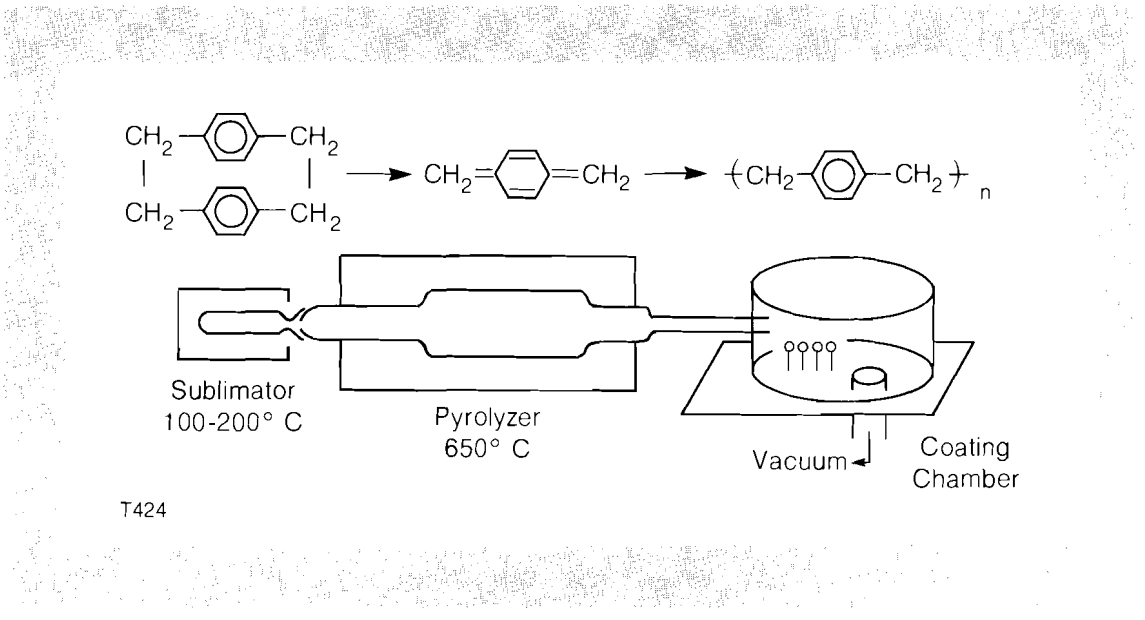

Fig. 25
The parylene process is used to coat laser-fusion targets with ablator layers. This system has been completely automated.

In the manual operation of the parylene coating system, the final coating thickness could be controlled only by maintaining a known deposition rate for a specified length of time. The deposition of a 10-μm coating, for example, required up to eight hours of careful work. This deposition rate was known only as an empirically derived function of the sublimation temperature and system pressure. Since these factors were both measured and controlled by an operator, the process was intrinsically time-consuming and approximate.

In the automated mode of operation, the parylene coater, by means of optical reflectometry, continuously monitors the thickness of the growing film on a glass "witness" slide placed in the coating chamber near the targets being coated. Extensive studies at LLE have verified that the coating thicknesses on the slide and on the targets are virtually identical. The parylene coating on the witness slide forms a multiply reflecting surface whose reflectivity to monochromatic He-Ne laser light (λ = 632.8 nm) varies sinusoidally with the increasing thickness of the coating. The modulation is caused by the interference between the reflections from the parylene/vacuum interface and the parylene/glass interface. This sinusoidal modulation advances one cycle for each thickness increment, Δt, equivalent to a half-wavelength in optical thickness, or $\Delta t = \lambda/(2n)$, where n is the index of refraction

of parylene (see Fig. 26). In the automated system, a microcomputer fits the reflectometer data to a $\cos^2(\pi t/\Delta t)$ function of the total thickness t, and thus continuously and accurately monitors the layer thickness. In contrast, an operator, by reading a strip-chart record of the reflectivity, can monitor the coating thickness only to within 1/8 of a cycle, or 25 nm of parylene. Although this accuracy is adequate for ablation-layer fabrication, a skilled operator is still needed to monitor the process parameters, do thickness calculations, and terminate the coating process when the appropriate thickness is reached.

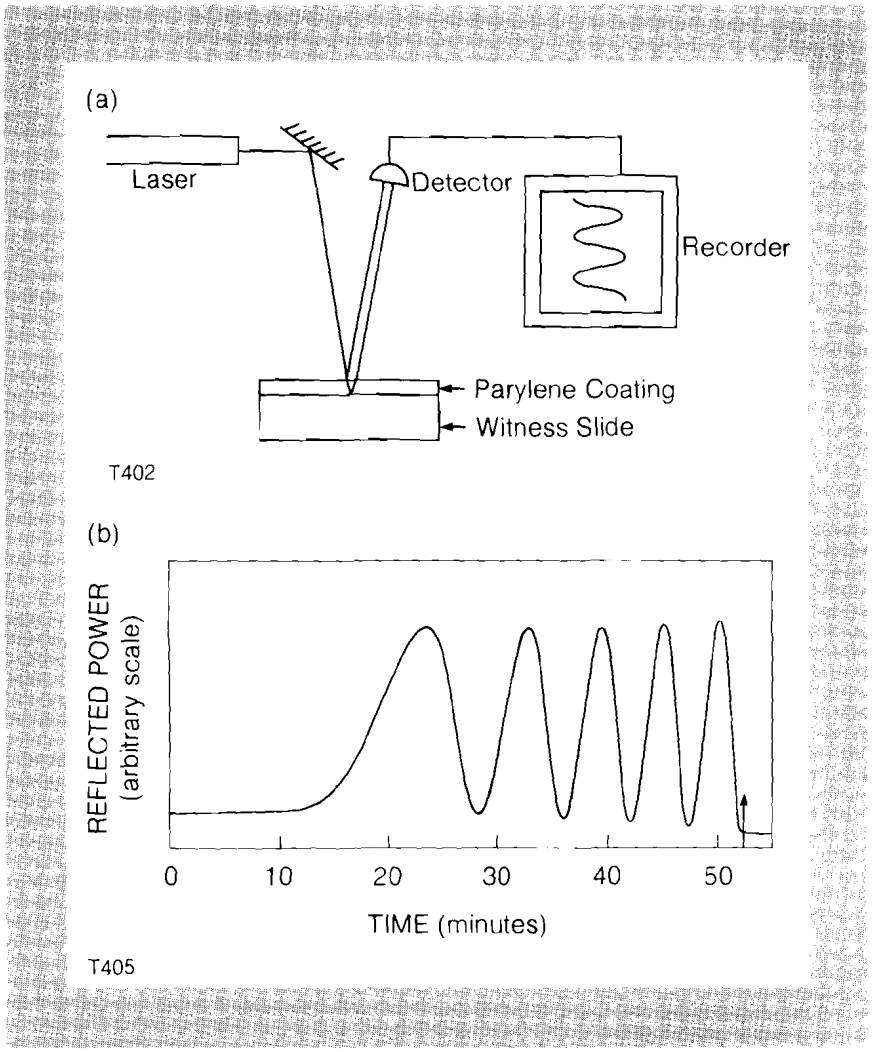

Fig. 26.
a) Optical reflectometry has provided a cost-effective method of real-time monitoring of parylene coating thickness.
b) Actual reflectometer output for a 1-μm film. The arrow on the reflectivity scan shows the time at which the sublimator was cooled. The fixing of the reflectivity value at this time indicates the rapid termination of the coating process.

The new, fully automated system performs all monitoring and safety functions. In addition to processing the reflectometer data, the microcomputer controls the sublimator heater, the sublimator cooling fan, and the sublimator and vacuum gauge heaters according to input from the reflectometer, the vacuum gauge, and the sublimator temperature sensor. Upon deposition of the desired thickness of parylene, the microcomputer activates mechanisms which remove the heater from the sublimator and turn on the sublimator cooling fan. This immediately terminates the coating growth and an alarm is sounded to notify the operator.

If, during the coating run, any of the process parameters deviate from threshold values or if critical components malfunction, appropriate alarms are sounded.

The parylene coater automation software was written in Forth.[5] Our system is "multi-tasked," meaning that the operator can change process parameters in the middle of a coating run.

The measurement and calculation functions of the automated system are affected by several sources of ambiguity. The index of refraction of parylene is known only to within 0.1%, which limits the resolution of the thickness associated with one complete reflectivity modulation cycle to 0.2 nm, assuming constant index of refraction as the film grows. The occasional variation in the reflectivity modulation amplitude from cycle to cycle has not been observed to exceed 5%, but this level of uncertainty gives an uncertainty in the modulation of 5% of the amplitude or 9° in phase. This phase uncertainty corresponds to a layer thickness uncertainty of 5 nm. Based on these estimates and estimates of other less important uncertainities, our best estimate of an achievable thickness specification is a tolerance of 10 nm. We have measured the thickness of target and witness-slide coatings with a Mach-Zehnder interferometer and have compared the results with reflectometer readings of target-coating thickness. The comparisons were completely consistent, to the precision of the Mach-Zehnder interferometer readings, which we also estimate to be near 10 nm.

Summary

The ablation-layer production facility has been automated. The new system performs a task virtually unattended that once required the constant attention of an operator for as much as eight hours per target. Thickness tolerances have been controlled to within 10 nm with the automated system.

REFERENCES

1. W. F. Gorham, *J. Polym. Sci.*, A-1, **4**, 3027 (1966).
2. LLE Review **1**, 40 (1979).
3. LLE Review **9**, 21 (1981).
4. LLE Review **13**, 12 (1982).
5. M. McCourt, "PDP-11 Forth-79 Implementation Guide," Laboratory for Laser Energetics Computer Systems Group Tech-Notes No. 1, 1981.

2.E Progress in Drill, Fill, and Plug Target Fabrication

The drill, fill, and plug technique was developed so that high-Z, slowly permeating diagnostic gases such as xenon and krypton could be contained inside glass microballoons (GMB's).[1,2] This fabrication

procedure involves laser-drilling a hole approximately 1 μm in diameter through the GMB wall, placing a quantity of low-melting-temperature solder-glass plug material loosely over the hole, filling the target in a pressure chamber, and applying heat to melt the plug, thus sealing the gas inside the target. Several changes and improvements in these procedures have been made and are reported in this article. The changes affect target quality directly and improve the efficiency of the operation by reducing losses at various stages of production.

Because inertial-confinement fusion targets require a high degree of spherical uniformity for optimum implosion performance, steps have been taken to reduce the mass perturbation caused by the solder glass used to seal the laser-drilled hole. Until recently, a plug (Fig. 27) typically had dimensions of 10-14 μm in diameter and 1-2 μm in height.[3] Plugs of this size were produced by fracturing a bubble blown from bulk solder glass. Perturbations are often evident in x-ray images of implosions of targets having plugs of this size.[4] Reduction of plug sizes to smaller diameters had been limited by a lack of plug material fragments of the appropriate size.

The production of plugs roughly 1.5 μm in diameter and 0.25 μm in height (Fig. 28) involves grinding solder glass fragments down to sizes that are only slightly larger than the laser-drilled hole in the GMB wall. Typically, reduced-size plugs have 300-600 times less volume than those produced using the fractured bubble technique. This results in a correspondingly smaller mass perturbation on an initially uniform shell. By this technique, about 50% of the GMB's are plugged successfully in any given heating cycle. This efficiency should improve as process capabilities are optimized for specific target parameters.

Improvements in the fabrication process include a variation of the salt-crystal bonding technique used to secure the target to a glass-slide substrate where it is held during the drilling, filling, and sealing steps. Previously, the target was secured to the glass slide with salt (NaCl) that was applied in solution with water. This method produced crystals which were ~ 25 to 50 μm in size. Crystals of this size worked well in securing GMB's up to ~ 200 μm in diameter.[3] For larger targets, however, the bond proved too weak to keep the targets secured during the heating stage of the process.

Successful bonding of 400-μm targets has been accomplished by sieving NaCl crystals to specific sizes and manipulating them into a tripod support configuration on the glass slide. The moisture necessary to initiate the bond is supplied by very light breathing through a plastic tube onto the crystals. Characterized GMB's are then secured by placement on a set of re-moistened crystals that bond the target to the slide once the evaporation of the applied water is complete.

Improvements in the gas handling system have also been attained by implementation of a reduced-volume gas manifold and valves. The system now requires approximately one-tenth of the gas previously necessary for operation. Also, pump-down and pressurization are more carefully controlled by a reduced flow rate through the system.

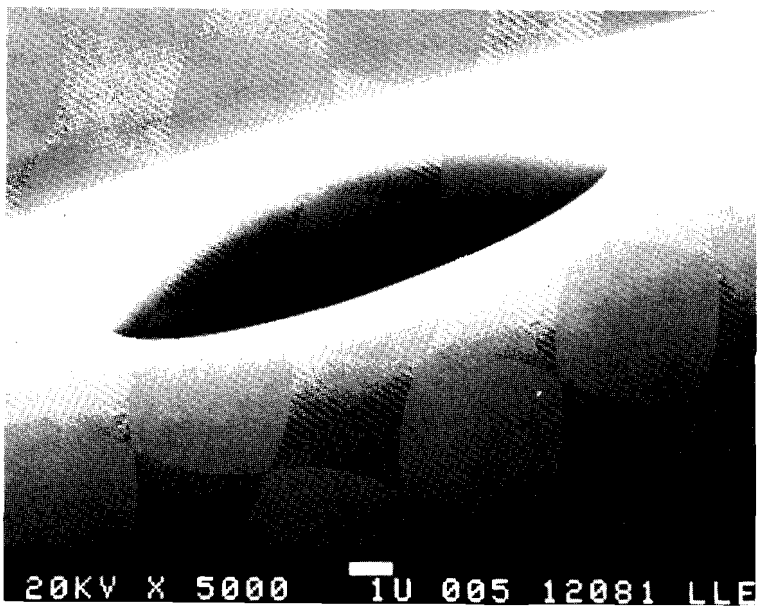

T440

Fig. 27
Scanning electron micrograph of a large plug, 14 μm in diameter, applied to a microballoon using the original technique.[3]

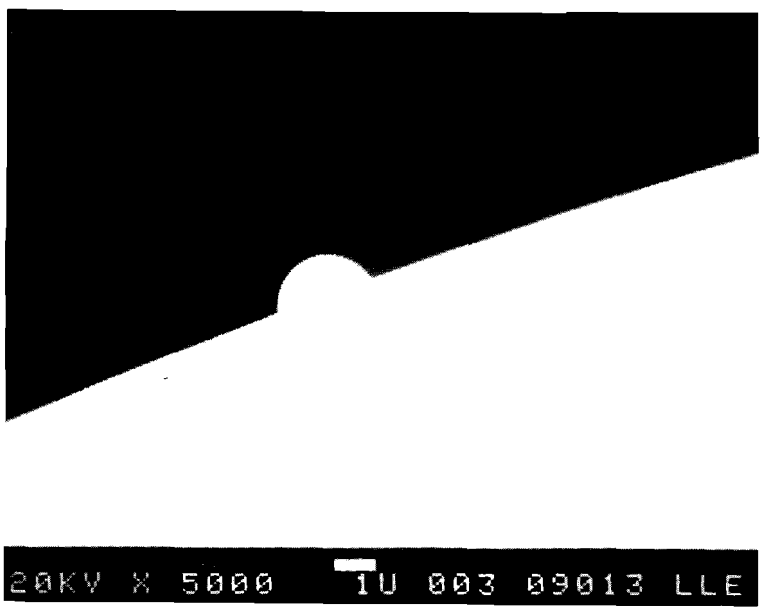

T563

Fig. 28
Smaller plug, 1.5 μm in diameter, applied to an identical microballoon using the improved technique (same length scale as in Fig. 27).

The main significance of our progress thus far is that we have passed out of the regime of gross shell nonuniformities. The implications for high-compression target implosions of the plug-mass and size reductions we have achieved are encouraging. The plug-mass reduction from approximately 0.4-1 ng to 2 pg and the corresponding reduction in areal density from approximately 4-8 pg/μm^2 to 1 pg/μm^2 is an important step. The plug masses are now sufficiently small that they are comparable to the mass lost in drilling through the shell.

Summary

The drill, fill, and plug target fabrication capability has been improved so that the fill-gas consumed is reduced by an order of magnitude, and the mass perturbation of the plug has been reduced by at least two orders of magnitude. This increased target uniformity should contribute significantly to the success of high-compression implosion experiments.

REFERENCES

1. S. Butler and B. Cranfill, *Technical Digest of Topical Meetings on Inertial Confinement Fusion* (Optical Society of America, Washington, D.C., 1980), paper THB10.
2. H. W. Deckman, J. Dunsmuir, G. M. Halpern, and J. Drumheller, *Technical Digest of Topical Meetings on Inertial Confinement Fusion* (Optical Society of America, Washington, D.C., 1980), paper TUE3.
3. LLE Review **11**, 12 (1982).
4. LLE Review **12**, 12 (1982), cf. Fig. 10.

Section 3
ADVANCED TECHNOLOGY DEVELOPMENTS

3.A Picosecond Fluorescence of Biomolecules

Accurate determinations of biomolecular structures which participate in fundamental photoreactions are generally difficult to obtain by standard methods. Chemical analysis, x-ray diffraction, and electron microscopy all require reasonably large samples, and, in the case of x rays, the samples must be crystalline. Fundamental photoreactive structures usually contain a low density of interesting sites. In the case of photosynthetic membranes, for example, there exists only one "trap" (a site where a local energy minimum occurs) for each 300 chlorophyll molecules. The chlorophylls are usually bound into water-insoluble proteins which cannot be crystallized. Finally, the first reactions initiated by light are extremely rapid, often involving photolabile molecules, so that normal time-independent or time-averaged results are of no interest. These are the facts underlying the need for short-pulse excitation and very rapid detection in primary photobiology.

Fluorescence and related processes in a typical biomolecule are illustrated in Fig. 29 by a standard configuration coordinate diagram. The horizontal axis represents displacement along some important structural degree of freedom. Fluorescence begins with an excitation by radiation (A→B). Process B→C is an excited-state relaxation which occurs typically in a few picoseconds or less. The discussion in this article centers largely on the observation of state C by means of fluorescence emitted in the decay C→D. Relaxation to highly distorted or ionized states may also take place (B→E) on a picosecond time

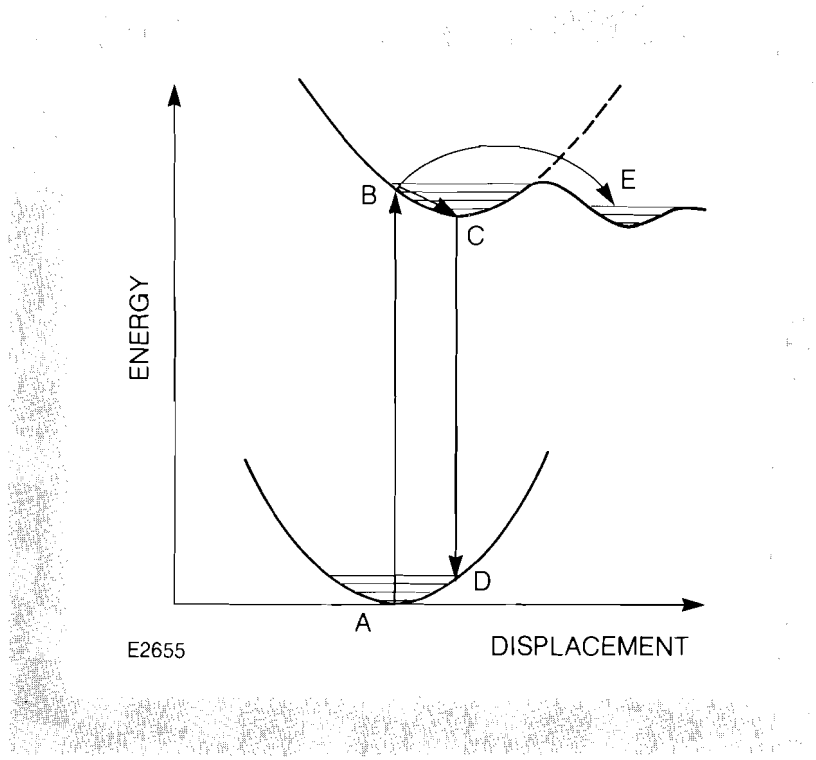

Fig. 29
The states of a molecule initially excited by radiation (A→B) can be sketched on a standard configuration coordinate diagram. The horizontal axis represents the displacement in some important structural mode. Process B→C is excited-state relaxation. Process B→E, where E may involve a highly distorted molecule or an ionized state, also may take place. State C is observed by means of fluorescence emitted in process C→D.

scale. In the experiments described below on primary processes in photosynthesis, the intensity of the fluorescent emission from a given transition C→D is used as a measure of the population of state C. In the second set of experiments on rapid changes in large-scale molecular structure, changes in the polarization of the fluorescent emission, relative to the polarization of the stimulus radiation, are used as a measure of the change in orientation of fluorescing sites on a macromolecule.

The experimental setup shown in Fig. 30 consists basically of a pulsed excitation source, sample, and streak-camera detector capable of 1-ps time resolution.[1,2] The pulse source is an actively and passively mode-locked Nd:YAG laser from which a single 30-ps, 1060-nm pulse is selected (by two Pockels cells in series) and amplified. This pulse triggers the jitter-free, signal-averaging streak camera and, after frequency conversion in crystals (2ω and 4ω), excites the sample. Fluorescence emission by the sample is filtered and imaged onto the streak tube. The streak image is intensified and the data is recorded by an optical multichannel analyzer (OMA). The 4ω crystal, the polarization rotator [Babinet-Soleil (B-S) compensator], and the polarizers are used when the anisotropy of the fluorescence is being measured.

The most relevant photophysical processes occurring in the systems currently under study by users at the LLE picosecond facility are excited-state relaxations within the original manifold of states (B→C in Fig. 29), intermolecular excitation transfer at very small distances such as 1.5 nm, primary electron transfer, and rapid rotation of small fluorescing chromophores (those segments of molecules which absorb

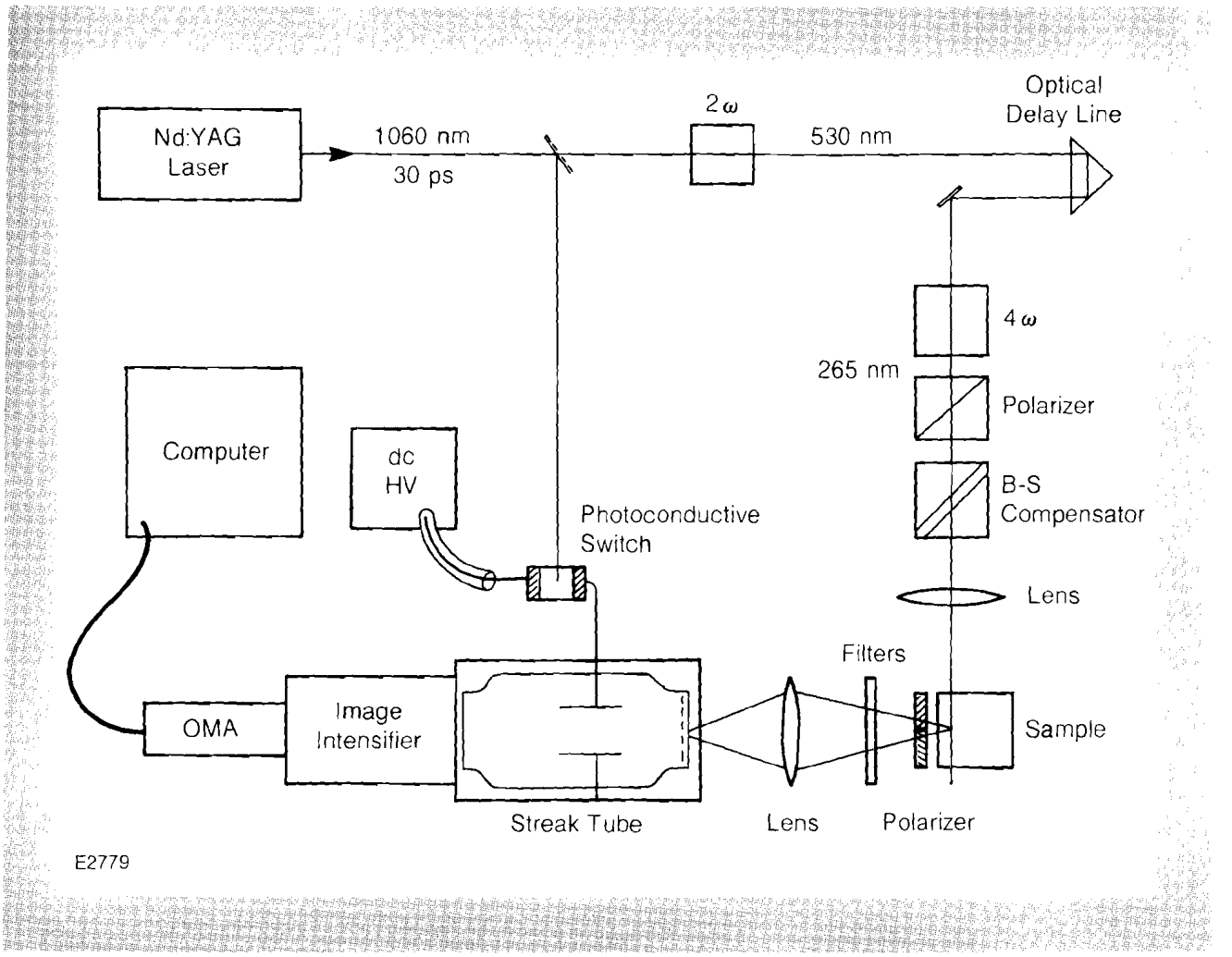

Fig. 30
Schematic of low-jitter, signal-averaging streak camera. A single 1060-nm laser pulse triggers the streak camera, and, after frequency conversion in crystals (2ω and 4ω), excites the sample. Fluorescence emission from the sample is filtered and imaged onto the streak tube. The streak image is intensified and recorded by an optical multichannel analyzer (OMA). The 4ω crystal, polarization rotator [Babinet-Soleil (B-S) compensator], and polarizers are used when the polarization anisotropy of the fluorescence is being measured.

and emit light efficiently) in large macromolecules. The first two of these are known to occur in times of the order of or shorter than 1 ps, while the latter two are in the 1- to 1000-ps range. We have also been studying multiple-excitation transfers on time scales of up to 100 ps, which may be thought of as a diffusion of excitation in a "pool" of chromophores.

While photophysical studies of primary photobiological function may be used to infer structures, it must be noted that such inferences are indirect and in most cases will lead only to the relative orientations of the chromophores involved. However, a more complete picture may emerge when these results are combined with those of more conventional studies of structures.

Research on the Primary Processes of Photosynthesis

The short-pulse detection systems at LLE have been employed to examine the fluorescence from chlorophyll-proteins[3], spinach chloroplasts, and algae. The object of the present research has been to elucidate the physical pathways by which excitation energy is delivered to reaction centers. The various types and functions of these centers are described in Fig. 31. It is now well-established that the

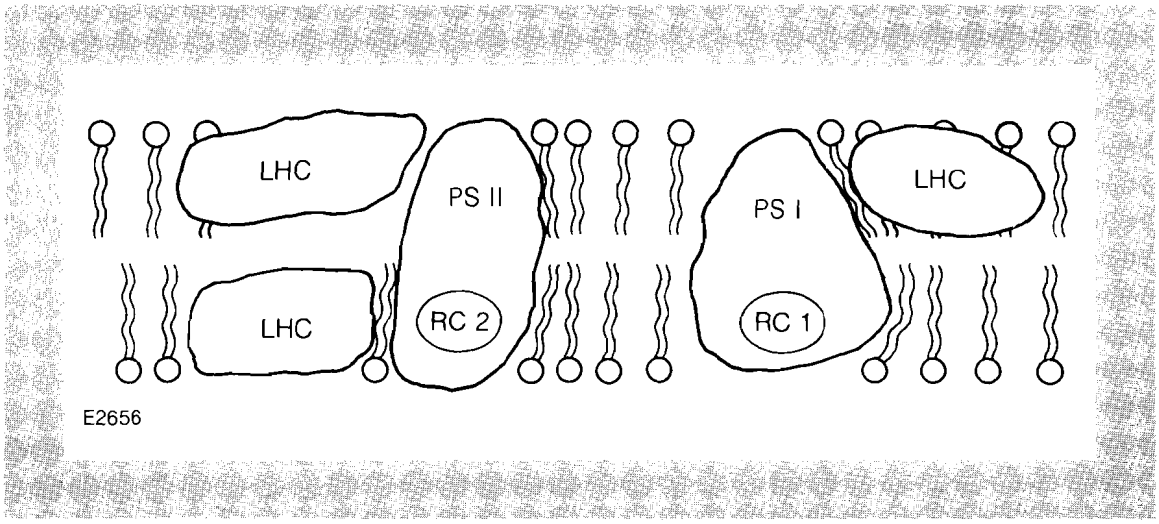

Fig. 31
Schematic cross section of the photosynthetic membrane. Chlorophyll protein LHC (light-harvesting chlorophyll) acts as a photon gatherer; protein complexes PS I and PS II (photosystems I and II) act both as light-gatherers and as loci of photochemical reactions. The small molecules with "tails" represent lipids arranged in a bilayer of thickness about 10 nm. Excitation is funneled to the reaction centers (RC1 and RC2), which energize a long sequence of oxidation-reduction reactions involving numerous intermediates (not shown). In some theoretical models of the primary process, LHC acts also as a medium for transferring excitation energy from PS II to PS I, and in some models, the LHC may move about in the membrane and assist either PS I or PS II in gathering energy.

chlorophyll molecules participating in the primary processes are organized by binding into proteins which are, in turn, imbedded in lipid-bilayer membranes.[4] The details of the chemical steps subsequent to delivery of the excitation energy to the reaction centers are beyond the scope of this review, but we may note that the principal results of the illumination of the structure are the development of a proton gradient across the membrane, oxygen production on one side, and the production of high-energy reductants on the other. The latter ultimately reduces carbon dioxide to starches and sugars in green plants.

After excitation by a visible light pulse, any of the chlorophyll-containing materials mentioned above emits in the region of 685 nm. At liquid nitrogen temperature, a new emission band apparently originating in PS I appears at 735 nm in leaves and chloroplasts (see, e.g., Ref. 5). These emission bands have long been considered as indicators of excitation present in PS II and LHC (685 nm) or in PS I (735 nm).

The research reported here[6] links several earlier approaches. By single-photon counting techniques the low-intensity excitation regime ($\lesssim 10^{12}$ photons cm^{-2} per excitation pulse) has been explored (see, e.g., Ref. 7). Experimentation in this regime has the advantage of being closest to true physiological conditions, but it cannot make use of fluorescence quenching by exciton collisions as a probe, as has been done in the much higher-intensity regime ($\gtrsim 10^{14}$ in the same units).[5] Research in this regime, however, has been limited to studies of total fluorescence yields as a function of intensity and to single-shot or crudely averaged time-course measurements.

Using 30-ps pulses of 530-nm light obtained by frequency-doubling the output of the Nd^{3+}:YAG laser, we have made a long series of measurements of the time-resolved fluorescent response of spinach chloroplasts. Figs. 32(a) through 32(c) summarize the principal results that demonstrate the indirect excitation of PS I and the fluorescence quenching of LHC and PS II at high excitation intensity. The fluorescence time courses have been analyzed in terms of a kinetic scheme

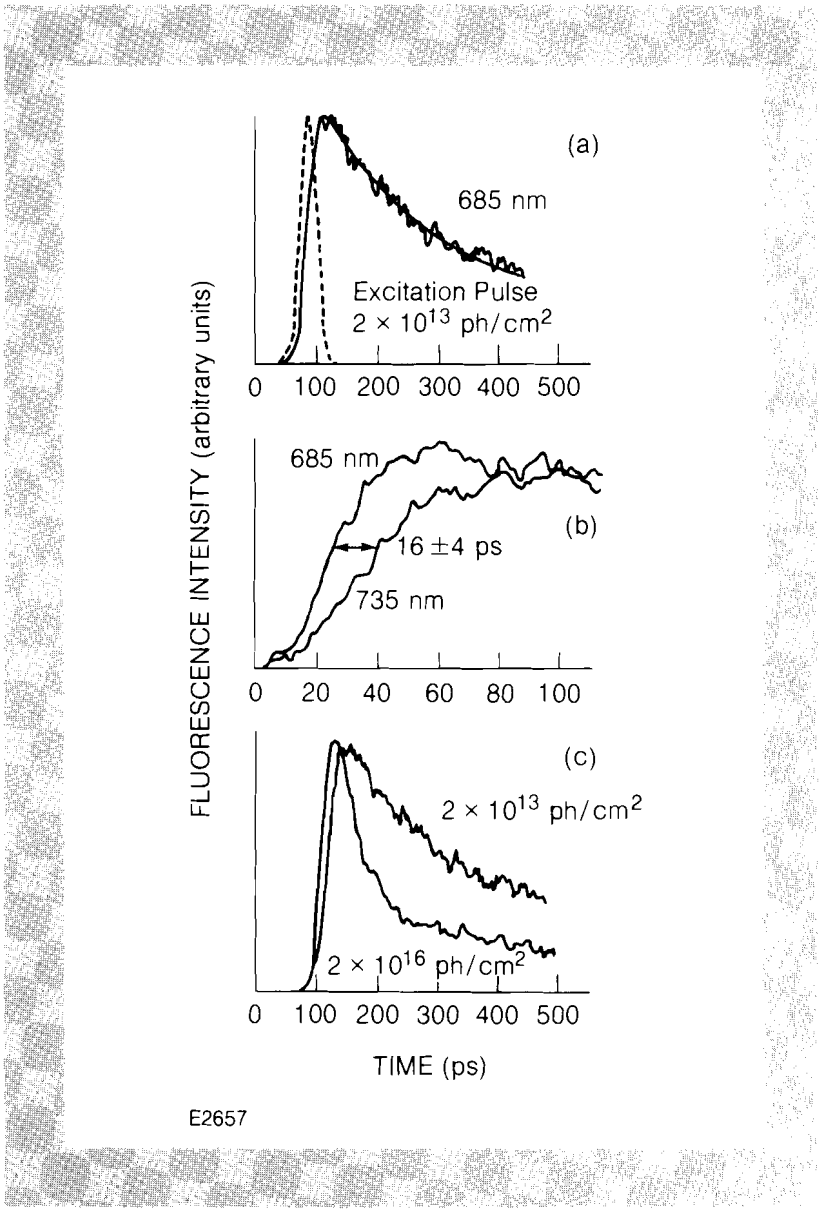

Fig. 32
Fluorescence response of chloroplasts at 77K to a light pulse.

a) Emission of light by spinach chloroplasts in the far-red (685 nm), upper curves, is the result of excitation by a 530-nm pulse, shown by the lower-left curve. The smooth curve is the response expected on the basis of photon-counting results. The 200-shot average response measured by streak camera, the other upper curve, is in close agreement despite high-level excitation at 2X10[13] photons/cm[2] per pulse.

b) The fluorescence at 735 nm, arising from PS I, is seen to be slightly delayed with respect to the 685-nm fluorescence. This fact, along with its rather biphasic rise, indicates that the 735-nm-emitting species receives its excitation indirectly. The excitation of the system was the same as in (a).

c) The 685-nm fluorescence decay acquires a more rapid decay in the 50-ps region when the excitation, otherwise the same as in (a), is made 1000 times more intense. The more rapid decay indicates the premature disappearance of excitons as a result of their colliding with each other at high densities (the process of exciton annihilation).

which accounts for exciton collision effects and corrects for other important nonlinear phenomena. The principal successes of this research are the repeatability of the experiments, the observation of nonexponential portions of the decays, the connections made with previous work, and the possible resolution of some conflicts in the literature.

Work on the photosynthetic apparatus will continue. With both the samples and the detection system now well-characterized, our emphasis will switch to greater spectral resolution and to determining the effects of ion concentrations and different degrees of membrane phosphorylation (chemical addition of phosphate groups to membrane components). The known effects of these physiological variables on membrane configurations can be correlated with their effects on the fluorescence and used for more detailed tracing of excitation pathways.

The study of the primary photoreactions of photosynthesis just described makes use of a direct measurement of the populations of various electronically excited states of chlorophylls from their fluorescent emission. In the work described below, we are interested in fluctuations and motions of the conformation (structure) of large biological macromolecules (polymers). In this case, the fluorescence of small chromophores located in various parts of the macromolecule indicates more indirectly the quantities of interest, namely how fast and by how much the conformation fluctuates. The amplitude and decay rate of the anisotropy (or polarization) of the chromophore fluorescence gives us both quantities. The chromophore's electronic excited-state population, of little interest in itself, serves as a probe of the mechanical-conformational states of the macromolecule.

Probes of Rapid Motion in Biological Macromolecules

Typical macromolecules found in nature can exist in an enormous number of conformational states of roughly the same energy. The two most common examples are the large, polymeric molecules called proteins (polypeptides) and DNA and RNA (polynucleotides). A polypeptide or polynucleotide with N units has roughly e^N such states.[8,9] If $N \approx 200$ (typical polypeptide), there are 10^{90} states; if $N \approx 10^4$ (typical polynucleotide), there are $10^{4,000}$ states. Transition from one state to another can occur when fluctuations cause one unit to move from or rotate about its previous position. Correlated motions of many units can also occur because of the relatively small number (on a macroscopic scale) of atoms involved. The correlated motions can alter enough of the macromolecule to allow water and other physiologically important molecules to move through a previously blocked section of the macromolecule, for example. Measured time scales for motions (fluctuations) range from less than one nanosecond for elementary motions to milliseconds to hours for major conformational changes. The fluorescence depolarization work described below was undertaken to clarify the extent and rate of the fast elementary motions and their dependence upon environmental factors such as temperature, solvent, pH, etc., which alter the biological activity of the macromolecule.

Motional depolarization of fluorescence emission from small chromophores can occur in less than 10 ps, whether the emitter is rotating in solution or executing restricted rotation at a site within a larger macromolecule such as a protein. Measurements on proteins[10] and polynucleotides,[11,12] limited in time resolution to 100-200 ps, have demonstrated motions of bound chromophores as fast as 100 ps, and suggested processes of about 10 ps. To achieve better time resolution we have employed the low-jitter signal-averaging streak-camera system described above which allows simultaneous recording of both emission polarizations in order to achieve good signal-to-noise ratios in determining the fluorescence anisotropy. Both the 2ω and 4ω crystals shown in Fig. 30 were used to convert the laser's fundamental wavelength, 1060 nm, to 265 nm. In one data-collection mode the emission polarizer was cut into two parts. One was oriented horizontally and collected emission from the half of the sample where the laser beam entered. The other was oriented vertically and collected emission

from the other half of the sample. The emission collection lens imaged both halves of the cuvette onto the streak-camera photocathode. The fluorescence anisotropy, defined as

$$r(t) = \frac{I_V(t) - I_H(t)}{I_V(t) + 2I_H(t)}, \quad (1)$$

where $I_V(t)$ is the vertically polarized emission and $I_H(t)$ is horizontally polarized emission (with vertically polarized excitation), decays when the initial preferentially vertical orientation of the excited molecules begins to randomize rotationally.

Human serum albumin (HSA) is a common protein of molecular weight 69,000. It is made up of about 600 amino-acid units. One of these amino-acid units is tryptophan, which fluoresces when excited with ultraviolet light. In Fig. 33 we use this fluorescence to measure the motion of this tryptophan as a function of temperature and solvent. One might expect more and faster motion at higher temperatures. A change in tryptophan's freedom to move might also be expected when a chemical agent such as guanidine hydrochloride is added to unwind the polypeptide chain. In Fig. 33, we find clear time resolution of a fast anisotropy-decay component which develops in HSA at high temperature (320K). This motion is not observed at room temperature (295K). The decay time of the fast motion is about 150 ps; the rotational angle corresponding to the amplitude is about 30°.[2] The slower component decays in at least 3 ns. This is similar to Munro's findings.[10] In the bottom of Fig. 33 we show that addition of guanidine hydrochloride to HSA does not affect r(t) in the same way as high temperature. The value of r(0) is lower, and a fast-decaying component does not appear to be present. The effect of the guanidine is probably due to changes induced in the electronic structure of the tyrosines and tryptophans in HSA. This can be checked by spectral measurements of absorption and fluorescence excitation.

Ethidium bromide (EB) is a dye molecule which binds between base pairs on a DNA chain. If the DNA undergoes torsional motion, the EB will rotate and the fluorescence anisotropy of the dye will decay. In this case we are adding our own chromophore to the macromolecule in order to monitor its motion. Figure 34 shows plotted a typical anisotropy-decay curve for EB bound to calf thymus DNA, together with the excitation light pulse. A fast decay component, roughly 100 ps, is apparent in our data. The theoretical curve was derived using the parameterization of Millar *et al.*[12] (see also Ref. 11) for the Barkley-Zimm[13] elastic-continuum model for torsional motion of DNA. Our data reveal the time course of an additional fast component not contained in the theory. Similar data were found for salmon sperm DNA, for DNA with varying ratios of EB to DNA, and for EB/DNA complexes in solvents of varying viscosities. This fast component may be due to the wobbling of EB within its binding site between two base pairs and not directly connected to the torsions of the DNA chain.

The ultimate importance of rapid internal motions to macromolecular biological activity remains to be determined. The question of the

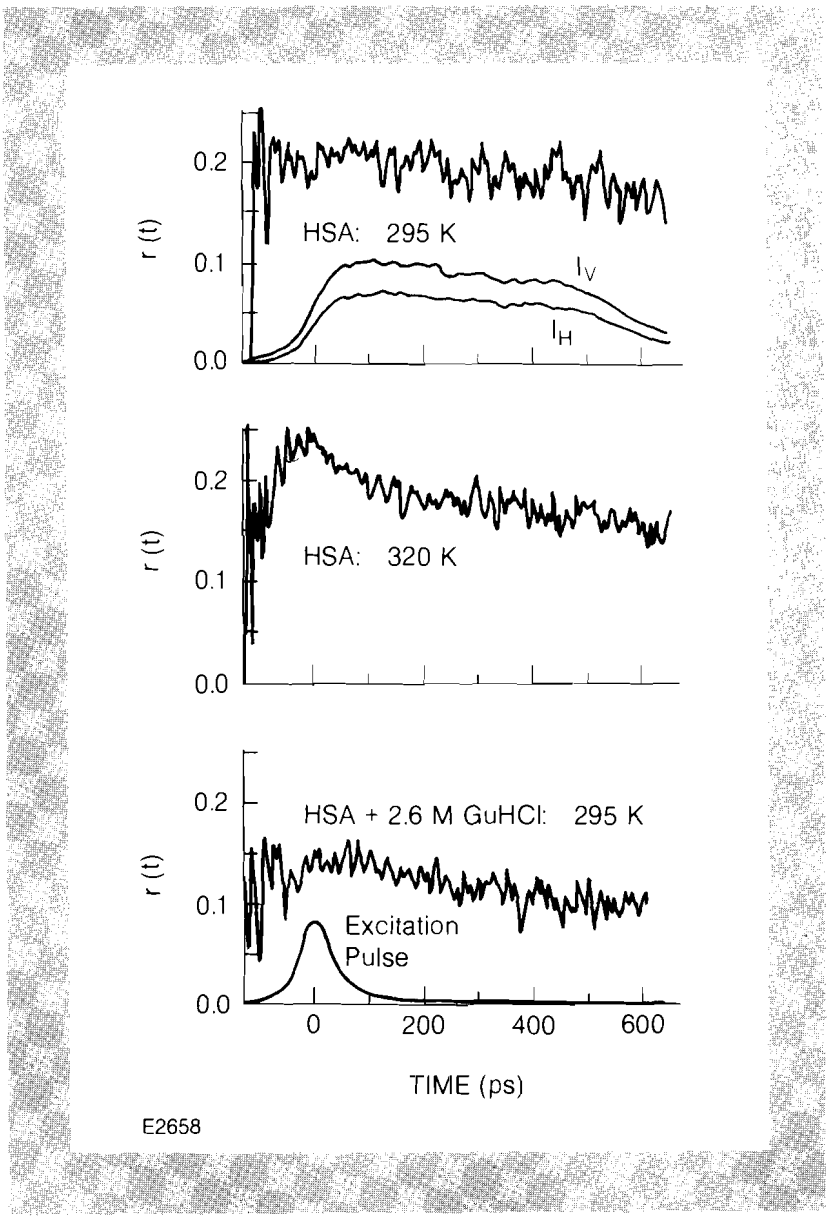

Fig. 33
Fluorescence polarization anisotropy decay from human serum albumin (HSA). The top figure shows the anisotropy at room temperature (295K), together with the vertically and horizontally polarized components of the fluorescence (arbitrary units). There is no fast motion. At 320K, there is fast motion (decay time about 150 ps) which may correspond to a restricted rotation through an angle of 30° (middle). Guanidine hydrochloride (GuHCl, bottom) unwinds the HSA protein chain. One naively expects more rapid, free motion. This is not observed.

correlation of rapid motions to those slower conformational changes known to be biologically significant (inhibitor-induced conformational changes in enzymes which alter reactivity, for example) must be thoroughly studied. It is clear, at least in the case of proteins, that fluctuations of a nanosecond time scale or less are involved in the binding of small molecules to certain proteins (oxygen to myoglobin, for example[9]; see also Refs. 14 and 15). The finding that the active sites of myoglobin and lysozyme contain mobile regions also provides a strong inducement to study the relation of enzymatic activity to fast internal motion. The elastic parameters of DNA (torsional rigidity and fluctuations in torsion angle) are important to know since they reflect base-pairing interactions which affect replication, transcription, and repair of the polynucleotide chain. The binding of mutagenic dyes, histones, and nonhistone proteins to DNA, which are involved in base-pair insertion or deletion, packing of DNA into compact packets, and

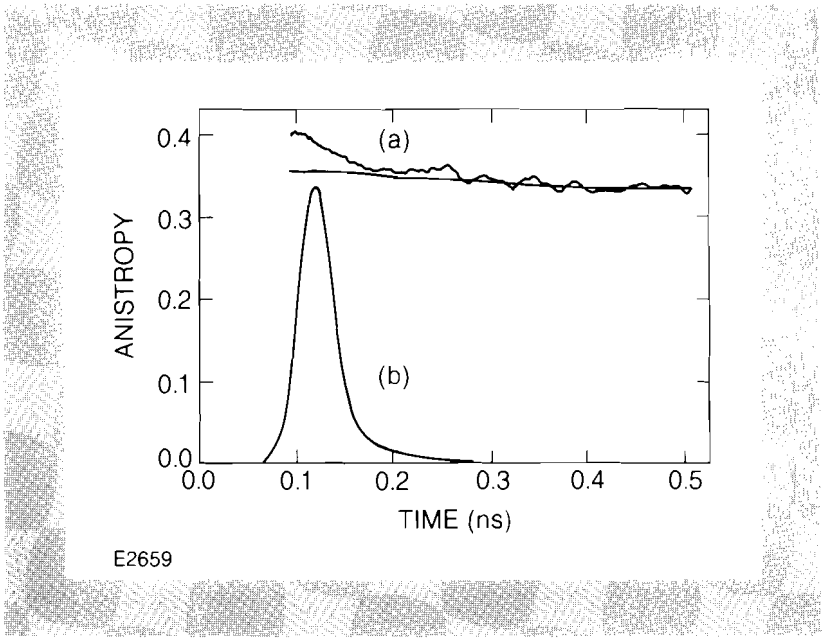

Fig. 34
Fluorescence polarization anisotropy results.
a) The polarization anisotropy decay of emission from ethidium bromide bound to DNA together with a smooth curve whose elastic-continuum-theory parameters have been chosen from a fit to earlier nanosecond data, convolved with instrument response.
b) Instrument response to exciting light (arbitrary units). The time origin is arbitrary.

control of gene function, respectively, must strongly affect the elastic properties of DNA. Finally, it must be kept in mind that, as is always the case with extrinsic fluorescent labels, fast motions may be indicative of label motion independent of the polynucleotide.

Summary

The observations of direct and indirect excitations within the photosynthetic membrane and rapid motion in macromolecules described here represent a sampling of the current picosecond photobiological research at LLE. They typify the application of picosecond techniques to a wide variety of biological questions. The results are being published in more complete form elsewhere.[2,6,16]

ACKNOWLEDGMENTS

The work reported in this article has been initiated and largely performed by users of the LLE picosecond facility and was supported in part by NSF grants which funded the establishment of a subpicosecond biological physics facility. University of Rochester users directly involved in this report are Professor Robert S. Knox and Mr. Bruce P. Wittmershaus, Department of Physics and Astronomy, and Professor Thomas M. Nordlund, of that Department and also of the Department of Radiation Biology and Biophysics. Outside users represented include Professors J. Breton (CEN-Saclay), N. E. Geacintov (New York University), and D. Magde (University of California at San Diego).

REFERENCES

1. LLE Review **11** , 26 (1982); W. Knox and G. Mourou, *Opt. Commun.* **37**, 203 (1981).
2. T. M. Nordlund and D. A. Podolski, *Photochem. Photobiol.* (1983, in press).
3. T. M. Nordlund and W. H. Knox, *Biophys. J.* **36**, 193 (1981).
4. Excellent reviews of the modern biophysical view of the photosynthetic membrane structure and function may be found in the series *Topics in Photosynthesis*, edited by J. Barber (Elsevier Scientific Publishing Co., Amsterdam). See especially *Vol. 3, Photosynthesis in Relation to Model Systems* (1979).
5. J. Breton and N. E. Geacintov, *Biochim. et Biophys. Acta.* **594**, 1 (1980).
6. B. Wittmershaus, T. Nordlund, W. Knox, R. Knox, N. Geacintov, and J. Breton, to be submitted to *Biochim. et Biophys. Acta.*
7. P. Reisberg, J. A. Nairm, and K. Sauer, *Photochem. Photobiol.* **36**, 657 (1982) .
8. L. D. Landau and E. M. Lifshitz, *Statistical Physics* (Addison-Wesley, Reading, Massachusetts, 1970), p. 15.
9. H. Frauenfelder, G. A. Petsko, and D. Tsernoglou, *Nature* **280**, 558-563 (1979).
10. I. Munro, I. Pecht, and L. Stryer, *Proc. Nat. Acad. Sci. USA* **76**, 56-60 (1979).
11. J. C. Thomas, S. A. Allison, C. J. Appellof, and J. M. Schurr. *Biophys. Chem.* **12**, 177 (1980).
12. D. P. Millar, R. J. Robbins, and A. H. Zewail, *Proc. Nat. Acad. Sci. USA* 77, 5593 (1980).
13. M. D. Barkley and B. H. Zimm, *J. Chem. Phys.* **70**, 2991 (1979).
14. F. R. N. Gurd and T. M. Rothgeb, *Adv. Protein Chem.* **33**, 73 (1979).
15. J. R. Lakowicz and G. Weber, *Biochemistry* **12**, 4171 (1973).
16. D. Magde, M. Zappala, W. H. Knox, and T. M. Nordlund, *J. Phys. Chem.* **87**, 3286 (1983).

3.B Picosecond Sampling with Electron Pulses

Recent advances in picosecond photodetector and photoconductive switching technology have created the need for a measurement system capable of accurately characterizing small electrical signals with picosecond resolution. To date, the best temporal resolution has been achieved using the picosecond electro-optic sampling system[1,2] developed at LLE. This device is based on the use of an electrical signal having an unknown temporal profile to modulate the intensity of a short optical pulse by means of an electro-optic crystal. An optical

pulse, of 100-fs duration, probes the change in birefringence of this crystal resulting from the electric field of the applied unknown electrical signal. This birefringence responds quickly (<100 fs) and linearly to the applied field. The optical probe pulse is short, compared with the typical duration of the unknown electrical signal (0.1 ps vs few ps), which allows for an accurate sampling of the signal's waveform to be taken. The most recent results from this system place the temporal resolution at 600 fs with a signal sensitivity of better than 50 μV. The electro-optic technique was reported in LLE Review, Volumes 11 and 13.[2]

At this time, we report on a new approach to signal sampling analogous to the electro-optic system. In this approach, electron pulses, rather than optical pulses, are used to interrogate the unknown electrical signal. This new technique, "electron-optic sampling," does not as yet allow as fine a time resolution as the electro-optic sampler. An important advantage of the electron-optic sampler over the electro-optic sampler, however, is that electrical signals in free space can now be investigated. Since electrons are charged particles sensitive to electric fields, a short electron pulse can act as a probe to monitor directly changes in the field.

The electron-optic sampler used in this work is illustrated in Fig. 35. A 100-fs optical pulse (at 610 nm) from a colliding-pulse mode-locked laser[4] is split in two with half the light directed between the electrodes of a GaAs:Cr photodetector biased to 30 Vdc. The other half of the pulse is frequency-doubled (to 305 nm) and directed onto the gold photocathode of the front end of a streak camera placed in vacuum (with the deflection plates removed), where the light pulse is converted into a sub-picosecond electron probe pulse.

The photogenerated electrical signal from the photodetector propagates in vacuum down a balanced-strip transmission line with no dielectric material between the plates. The electron pulse passes through the spacing between the plates of the transmission line assembly where the electric field from the electrical signal is established. When the electron pulse arrives in coincidence with the electric field, the electrons are deflected by an amount proportional to the electric field. This deflection results in the displacement of a spot on a phosphor screen placed in the path of the electron pulse. As in the electro-optic sampler, only a small segment of the total electrical signal is sampled at any one time. By changing the relative delay between this unknown signal and the electron pulse, a new portion of the signal can be sampled. In this manner, the full waveform of the unknown electrical signal can be mapped out.

There are several reasons why the front end of a streak camera tube is an ideal pulse source. Such a tube, in its usual mode of operation, converts short optical pulses into exact electron-pulse replicas, down to a single-picosecond time scale. The electrons are highly monoenergetic (one part in 10^4), and, in its present application, this tube gives picosecond or sub-picosecond electron pulses. The electrons are also easily imaged and capable of being pulsed at a rate

of 100 MHz. Due to the large repetition rate, only a few electrons per pulse are necessary to give a significant signal. Using, on the average, less than one electron per pulse, no temporal broadening by space-charge effects can occur, and tight focusing is possible. In the future, this feature could make possible the use of photogenerated electrons as a possible source for time-resolved scanning electron microscopy. In addition, and most importantly, the electron pulses can be synchronized to within 1 ps of the original pulse.[3]

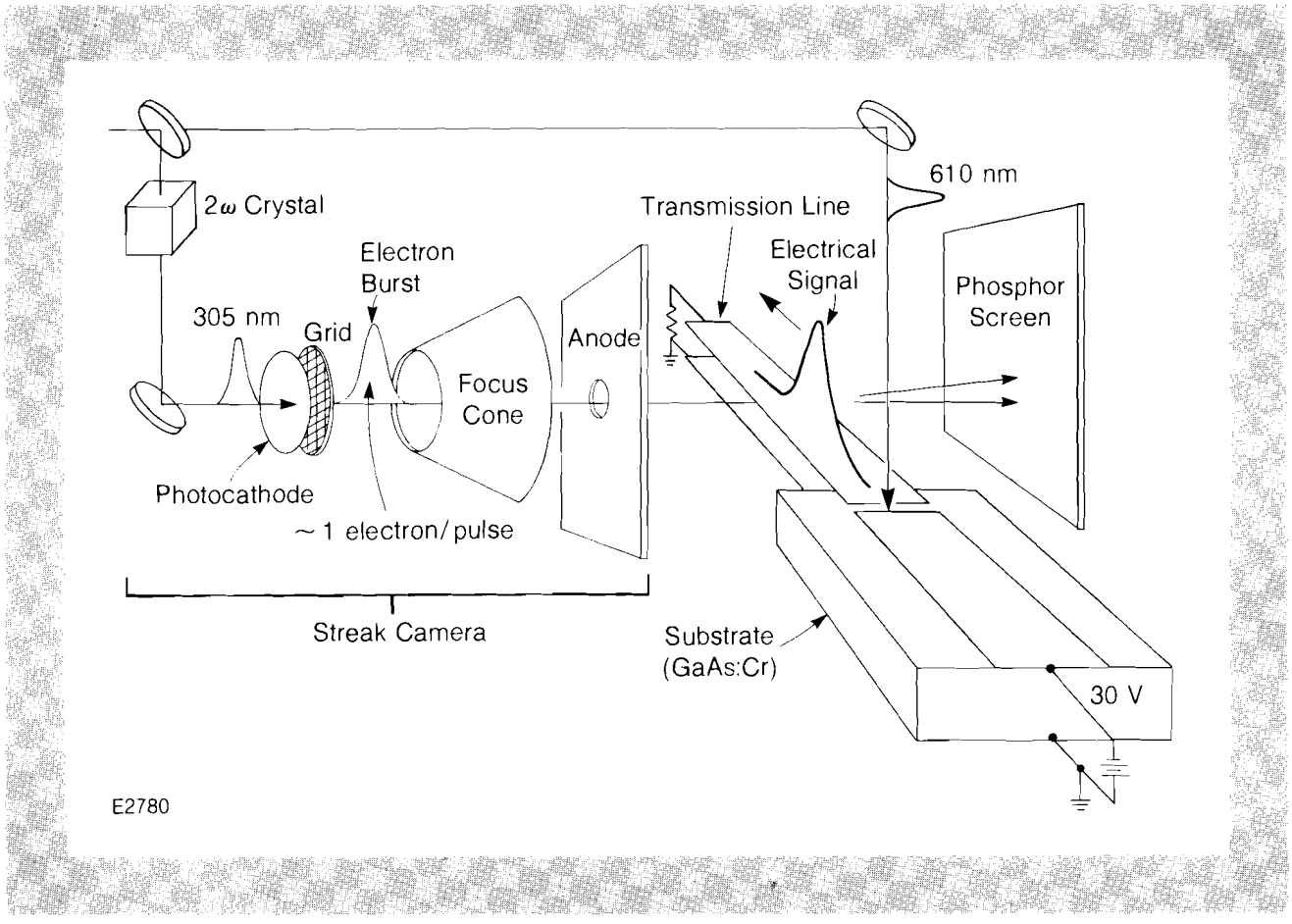

Fig. 35
Schematic diagram of the picosecond electron-optic sampler. A 100-fs optical pulse (at 610 nm) is split in two with half the light directed between the electrodes of a GaAs:Cr detector. The other half of the pulse is frequency-doubled (to 305 nm) and directed onto the gold photocathode of the front end of a streak camera. The electrical signal to be investigated propagates down the transmission line, establishing a traveling electric field between the two plates as it propagates. The field deflects the short electron pulse so that the spot on the phosphor screen is shifted by a small fraction of the spot diameter.

After passing between the transmission-line plates, the electrons are converted using a phosphor-screen/image-intensifier assembly back into a visible signal. The position of the deflected spot is read electronically. Displacements of less than one part in 10^3 of the spot diameter were measurable using a lock-in amplifier in conjunction with a signal averager. The result of this preliminary work is shown in Fig. 36. The 10-90% rise time is ~35 ps, which mainly corresponds to the electron transit time of the 20-keV electrons across the 2.5-mm deflection plate width. The maximum electron pulse deflection observed corresponds to a 1-V signal amplitude. The structure on the falling edge of the signal is the signal reflection due to the impedance mismatch at the point where the stripline leaves the substrate. Since the temporal resolution scales with the deflection plate width, the resolution of the system should be easily improved to the single-ps level by narrowing the deflection plates.

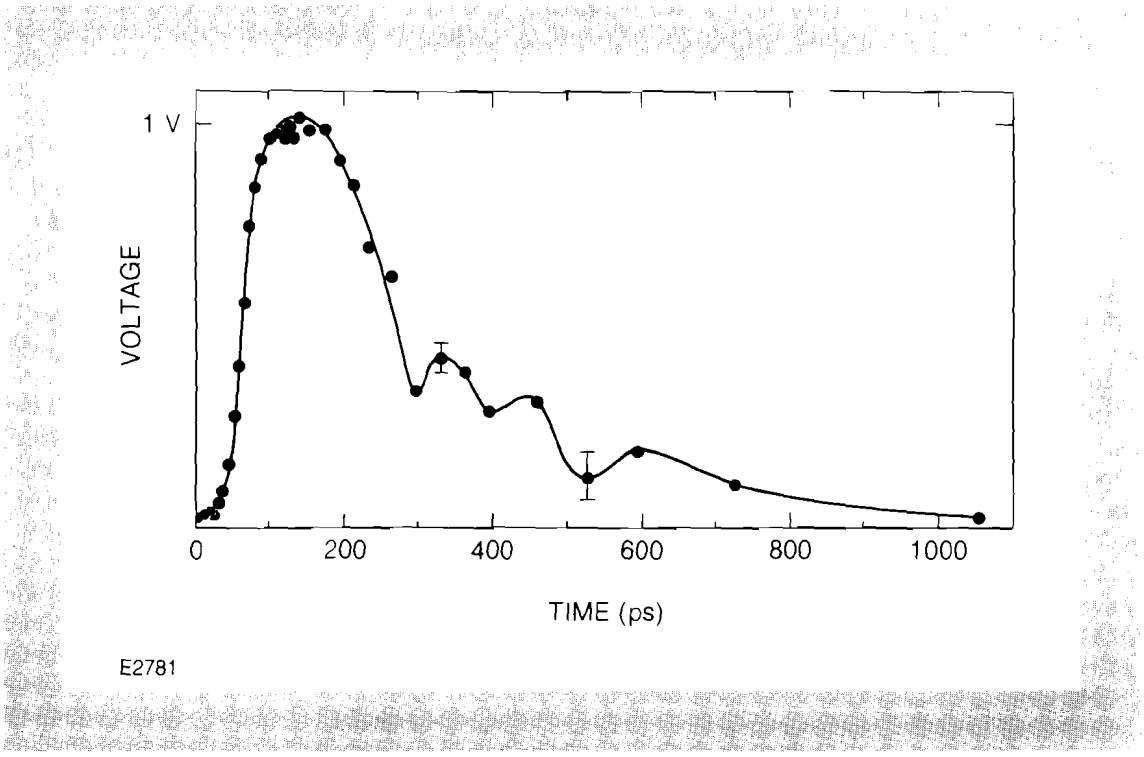

Fig. 36.
The rise time of the impulse response of the GaAs:Cr detector measured by the electron-optic sampler is ~35 ps. The maximum electron-pulse deflection observed corresponds to a signal amplitude of 1 V. The structure on the falling edge of the signal is due to the signal reflection off the impedance mismatch at the point where the stripline leaves the substrate.

The experiment described here restricts the electrical signal to a symmetric transmission line, but because the electron-optic sampler monitors the electric fields directly, it is possible to interrogate any electrical signal that radiates into free space. The electron-optic sampler will permit picosecond-scale sampling of electric fields radiating from radar antennas, the fringing fields of an integrated circuit, or simply the end of a coaxial cable.

Summary

The electron-optic sampler developed at LLE samples electrical signals directly by probing their electric fields with electrons. This method does not require crystals or any other device to be placed between the electric signal and the probe. In fact, free fields can be sampled. The temporal resolution for a signal of a few millivolts is approximately 35 ps, but a resolution of a few picoseconds appears possible in the near future.

REFERENCES

1. J. A. Valdmanis, G. Mourou, and C. W. Gabel, *Appl. Phys. Lett.* **41**, 211 (1982).
2. LLE Review **11**, 22 (1982); *ibid.* **13**, 44 (1982).
3. W. Knox and G. Mourou, *Opt. Comm.* **37**, 203 (1981).
4. R. L. Fork, B. I. Greene, and C. V. Shank, *Appl. Phys. Lett.* **38**, 671 (1981).

Section 4
NATIONAL LASER USERS FACILITY NEWS

This report covers the activities of the National Laser Users Facility (NLUF) during the quarter July to September 1983. During this period, four users conducted experiments on LLE facilities. The visiting scientists associated with these experiments represented the University of California at Los Angeles, Yale University, the University of Connecticut, the University of Pennsylvania, and the Naval Research Laboratory. These users conducted experiments on the Glass Development Laser (GDL), compiling a total of 69 shots. A specific listing of shots can be found in Section 1 (Laser System Report) of this issue.

The four user experiments on the GDL system used either 351-nm or 1054-nm laser light focused onto flat targets for either plasma physics or x-ray diffraction experiments. The participating individuals of each experiment are:

1. Francis Chen, Chan Joshi, Humberto Figueroa, and Ken Marsh (UCLA), and Nizarali Ebrahim (Yale University): "Studies of the Two-Plasmon Decay and Stimulated Raman-Scattering Instabilities in Hot, Long Scale-Length Plasmas."
2. Leo Herbette and Robert McDaniel (University of Connecticut): "Time-Resolved X-Ray Diffraction of Acetylcholine Receptor Membranes."

3. J. Kent Blaise, D. Pierce, Donatella Pascolini, and A. Scarpa (University of Pennsylvania): "Time-Resolved Structural Studies of the Ca^{2+}-ATPase of Sarcoplasmic Reticulum Membranes Utilizing a Laser Plasma X-Ray Source."
4. Raymond Elton, T. N. Lee, and Robert Denningham (Naval Research Laboratory): "Gain Measurements for a Soft X-Ray Laser High-Density Plasma Probe."

Additional information on these experiments can be obtained from the scientists associated with the experiment. Further information on the NLUF is available by writing to:

Thomas C. Bristow, Manager
National Laser Users Facility
Laboratory for Laser Energetics
University of Rochester
250 East River Road
Rochester, New York 14623

PUBLICATIONS AND CONFERENCE PRESENTATIONS

Publications

R. S. Craxton, "Interpretation of Livermore Third-Harmonic-Generation Experiments," *Appl. Opt.* **22**, 2739-2742 (1983).

S. Skupsky, "Uniformity of Energy Deposition for Laser-Driven Fusion," *J. Appl. Phys.* **54**, 3662-3671 (1983).

R. W. Short and E. A. Williams, "Brillouin Scattering of Multiline Laser Light in a Flowing Plasma Corona," *Phys. Fluids* **26**, 2342-2344 (1983).

B. Yaakobi, H. Kim, and J. M. Soures, "Submicron X-Ray Lithography Using Laser-Produced Plasma as a Source," *Appl. Phys. Lett.* **43**, 686-688 (1983).

S. A. Orszag, G. R. Baker, R. L. McCrory, D. I. Meiron, and C. P. Verdon, "Rayleigh-Taylor Instability of Ideal Fluid Layers," *Proceedings of the CEA/Los Alamos Meeting on Hydrodynamic Shock Waves and Instabilities*, Los Alamos, New Mexico, 28 June-1 July 1982, Paper 22 (September 1983).

R. L. McCrory, H. E. Trease, S. A. Orszag, and C. P. Verdon, "Hybrid Pseudospectral Techniques for Coupled Conduction-Hydrodynamic Flows in Multimaterial Media," *Proceedings of the CEA/Los Alamos Meeting on Hydrodynamic Shock Waves and Instabilities*, Los Alamos, New Mexico, 28 June-1 July 1982, Paper 23 (September 1983).

Forthcoming Publications

W. Knox and L. Forsley, "Data Acquisition System for a Jitter-Free Signal-Averaging Streak Camera," accepted for publication by the American Chemical Society.

B. Yaakobi, J. Delettrez, R. L. McCrory, R. Marjoribanks, M. C. Richardson, D. Shvarts, S. Skupsky, J. M. Soures, C. Verdon, D. M. Villeneuve, T. Boehly, R. Hutchison, and S. Letzring, "Thermal Transport Measurements in 1.05-μm Laser Irradiation of Spherical Targets," accepted for publication by *Physics of Fluids*.

J. A. Abate and R. Roides, "Spatially Resolved Absorption and Detection of Microscopic Impurities in Optical Thin Films by Photothermal Deflection," accepted for publication by *Journal de Physique Colloques (Photoacoustique)*.

J. Lubezky and A. Lubezky, "Antireflective Coatings Design Revisited," accepted for publication by *Optical Engineering*.

A. Simon, R. W. Short, E. A. Williams, and T. Dewandre, "On the Inhomogeneous Two Plasmon Instability," accepted for publication in *Physics of Fluids*.

S. Skupsky, R. L. McCrory, R. S. Craxton, J. Delettrez, R. Epstein, K. Lee, and C. Verdon, "Uniformity of Energy Deposition for Laser-Driven Fusion," *Laser Interaction and Related Plasma Phenomena*, edited by H. Hora and G. Miley (Plenum Press, New York, 1983, in press).

Conference Presentations

G. Mourou, "High-Speed Electrical Measurements" and "Ultrafast Electrical Transient Analysis with Picosecond Resolutions," presented at the NATO Advanced Study Lecture, Institute Castelvecchio Pascoli (Lucca), Italy, July 1983 (invited talk).

G. Mourou, "Electrical Pulse Shaping Using Frozen Wave Generator and Dispersive Transmission Lines," presented at Lawrence Livermore National Laboratory, Livermore, California, August 1983.

G. Mourou and J. Valdmanis, "Subpicosecond Electrical Sampling," presented at the SPIE Conference on Picosecond Optoelectronics, San Diego, California, August 1983.

R. L. McCrory, "Laser-Fusion Experiments and Theory at the Laboratory for Laser Energetics," presented at the Sixteenth ECLIM Conference, London, England, September 1983 (invited talk).

J. M. Soures, J. M. Forsyth, R. Frankel, M. C. Richardson, and B. Yaakobi, "Applications of Laser-Produced Plasmas," presented at the Sixteenth ECLIM Conference, London, England, September 1983.

J. P. Matte, T. W. Johnston, J. Delettrez, R. L. McCrory, and J. Virmont, "Electron Heat Flow with Inverse Bremmsstrahlung and Ion Motion," presented at the Sixteenth ECLIM Conference, London, England, September 1983.

The work described in this volume includes current research at the Laboratory for Laser Energetics which is supported in part by the Empire State Electric Energy Research Company (ESEERCO), the General Electric Company, the New York State Energy Research and Development Authority (NYSERDA), Northeast Utilities, The Standard Oil Company, University of Rochester, and various United States Government agencies, including the Department of Energy, the Air Force Office of Scientific Research, the National Institutes of Health, and the National Science Foundation.